Stony Brook University

OFFICIAL COPY

Measurement of Vertically Aligned Carbon Nanotube Array Compression Response

A Thesis Presented

by

Changhong Cao

to

The Graduate School

in Partial fulfillment of the

Requirements

for the Degree of

Master of Science

in

Mechanical Engineering

Stony Brook University

December 2010

Stony Brook University

The Graduate School

Changhong Cao

We, the thesis committee for the above candidate for the

Master of Science degree,

hereby recommend acceptance of this thesis.

Dr. Chad S. Korach, Advisor, Mechanical Engineering

Dr. Imin Kao, Chair, Mechanical Engineering

Dr. Robert Kukta, Member, Mechanical Engineering

This thesis is accepted by the Graduate School

Lawrence Martin

Dean of the Graduate School

Abstract of the Thesis

Measurement of Vertically Aligned Carbon Nanotube Array Compression Response

by

Changhong Cao

Master of Science

in

Mechanical Engineering

Stony Brook University

2010

The use of carbon nanotubes (CNTs) in the form of vertically aligned arrays or films has been of interest due to the super-compressible response and the ability to be used as electrical and thermal contacts. CNT arrays have shown the remarkable ability to react as foam-like structures and exhibit localized, coordinated buckling within specific regions. An understanding of the buckling region evolution and the resulting effects on the bulk CNT array

iii

response are important, unanswered fundamental questions necessary for the future application of CNT arrays. Here, we report on the low-cycle compression of bulk vertically aligned CNT arrays to observe initiation and growth of the buckling as a function of compressive strain and the contacting substrate material. A critical strain of ~5.5% is found above which the buckling region length increased and below which remained at or below the applied strain. The results are corroborated with nanoindentation on the surfaces, which indicate a stiffening of the near surface by 9.4%-16.5% with increasing applied strain. Also, contact counterfaces with different stiffness, lithium niobate and a polymer gel, were compared, which resulted in changes of ~32% in total array height after cyclic compression. Raman spectroscopy on CNT arrays before and after compressive deformation was performed observing repeatable vibrational shifts in the strained regions. Also, to observe the applicability of CNT arrays as contact sensors, electrical resistance change during compression was measured and found to increase by 4 times in the parallel versus vertical direction. Observation and results of the buckling region nature and relationship with applied strain and contacting substrates are important for applying the nanotube arrays to energy absorbing cushions, tunable dampers, thermal contacts, contact sensing, chemical sensing, or in sliding contact.

Dedicated to the Lord and My Families

Table of Content:

List of Figures

Acknowledgement

Chapter One - Introduction

The use of carbon nanotubes (CNTs) in the form of vertically aligned arrays or films has been of interest due to the super-compressible response [1] and the ability to be used as electrical [2] and thermal [3] contacts. Because of the high elastic modulus, tensile and flexural strengths [4-10], CNTs have many significant features for mechanical applications. The mechanical properties of individual carbon nanotubes have been characterized in compression [11, 12] and in tension [13], as well as mechanical characterization of composites made of dispersed CNTs at low loadings [14-17]. However, analysis of mechanical properties of oriented CNT arrays are only now becoming of more interest. CNT arrays or forests have been annealed to show an increased stiffness [18], measured the contact resistance of [19, 20], the viscoelastic nature and fatigue resistance have been characterized [21], contact wetting angles on compressed surfaces have been measured [22], tribological properties considered [10], and have been made into continuous CNT composites [23] and multifunctional brushes [24]. In addition, mats or films of unorganized CNTs have been characterized for their compressive properties [25]. A unique observation from the compression of organized VACNT arrays is the localized, periodic buckling which occurs during loading (Fig. 1.1). The buckling is coordinated and occurs only in specified regions of the array. This is of particular interest due to the effects on contact

conditions for the use as cushions, brushes, or electrical contacts. Observations of the buckling have been limited, but multiple end conditions have been studied. Cao et al. [1] have observed buckling with a fully released free film (two free surfaces), where Zbib et al. [26] and Tong et al. [27] both fixed one surface. Pushparaj et al. [2] fixed both ends as well as Deck et al. [28] (who also tested compression of fully released films, though did not report buckling), allowing tensile testing. Various strains were applied by all authors ranging up to 85%. As well as varying strains, the range of array geometries has varied from heights of 15 μm to over 3mm, and the height effect has been studied in detail by Tong et al. [27]. Regardless of the different conditions for testing, not to mention the variability in fabrication techniques, two salient observations can be made from these studies, 1) the measured buckling period is consistently 10 – 12 μm, and 2) that coordinated buckling of the CNT arrays occurs always at the tube end in contact with the growth substrate. Though the buckling period has been measured by SEM, and the total height change measured as a function of loading cycles, the size of the buckling region has not been characterized as a function of loading cycles. This is particularly important for an understanding of the long term performance of the arrays when used in contact conditions. For example, Cao et al. [1] measured the high cycle (1000 cycles) response of CNT array forests to strain observing the beginning of an asymptotic relationship between deformation change and cycles; others [2, 26-27] have applied a single or an unknown number of cycles and have not quantified the extent of the buckling region. This thesis reports the length of the buckling region and the total array deformation as a function of low-cycle compression for a VACNT array in contact with a stiff (LiNbO$_3$) material and a compliant (Gel polymer) material; where the

2

contacting side of the array was released from the growth substrate and contains the buckling region. A critical buckling region length scale of 75 µm is identified, which above controlled and uncontrolled buckling may occur depending on the applied strain.

The effective modulus of VACNT arrays have been characterized using nanoindentation [29, 30], and nanoindentation also utilized to observe buckling of thin CNT films [31]. However, indentations on the buckled or compressed turf were never mentioned, and present a method to characterize changes within the near-surface of the VACNT in contact with a substrate. Here, nanoindentation is used on the surface of the arrays to characterize the effect of compression on the effective stiffness of the VACNT array for different applied strains.

Raman spectroscopy is a powerful and popular technique to study vibrational properties and electronic structures of CNT [32, 33], particularly for characterization of the diameter distribution, chirality, purity, and architecture [34, 35]. Various carbon materials have been analyzed by Raman spectroscopy including single-walled (SWCNT) [36], double-walled (DWCNT) and multi-walled (MWCNT) carbon nanotubes [37, 38] and for arrays and composites of CNTs [39]. However, the Raman features of CNTs under strain are relatively unexplored. Rajay [40] has applied tensile strain on a SWCNT bundle up to 17% strain and observed Raman spectra changes indicating a debundling of the nanotubes. The Raman frequencies associated with the graphitic band are found to decrease with applied strain due to the elongation of the C-C bond and radial breathing modes (RBM) are found to increase, indicating a strain-induced decoupling of nanotubes within the bundle. Raman characterization of MWCNT arrays under axial compressive strain is utilized here to explore the electronic

3

structure of the buckled region in Fig.1.1. Raman scattering Buckled and unbuckled regions on the side surface of the CNT array are characterized with Raman spectroscopy in order to observe the effects of plastic strain on the Raman features of the array, where discrete shifts have been observed.

A fundamental understanding of the compressive response of VACNT arrays contributes to the design of CNT-based sensing systems, for the use in tactile, contact, and potentially gas sensing applications. CNT arrays may be utilized as strain gage sensors which have high gage factors due to the good piezoresistive properties of CNTs. The electrical response of CNT arrays has been used in electromechanical switches [41] where the effect of a mechanical perturbation drives the electrical response. Thus, the electrical responses of the array under compressive strain are of great importance and interest to study fundamentals of the electro-mechanics. Pushparaj [2] has measured the electrical conductivity of compressed CNT arrays and showed reversible conductivity and compressive strain responses in the elastic range of the array for both perpendicular and parallel tube directions. However, for sensing and control purpose, localized plastic deformation of the array occurs when loaded cyclically [1]. Here the electrical response of the CNT array under compressive strain is measured to determine relationships between the resistance changes with respect to the array deformation. A model of the geometry and resistivity effects on resistance change is presented, which captures the experimentally observed trends. Electrical conductivity measured in the perpendicular direction to the CNTs greatly enhances the response sensitivity with strain and provides a simplistic method for implementing CNT arrays as sensing devices.
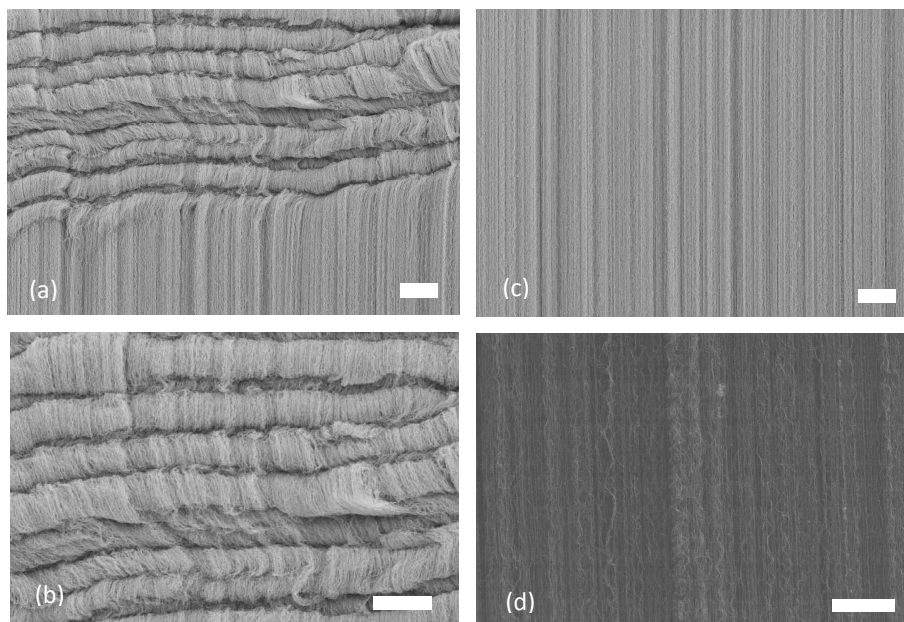
Fig. 1.1 – Scanning electron microscopy (SEM) of VACNT arrays: (A) Buckling region of the VACNT imaged after compression tests (10 cycles), compression applied by Si wafer (not shown) in contact with upper portion of array in the image, the buckling-to-straight CNT interface is presented in the center (10 μm scale bar); (B) Higher resolution imaging of VACNT buckling after compression (10 μm scale bar); (C) Side view image of uncompressed region in VACNT array (10 μm scale bar); (D) Image of uncompressed CNTs at higher magnification, showing entanglement of as grown tubes (5 μm scale bar).

Chapter Two - Compression Response of VACNT Array

In order to study the effects of VACNTs applied to compression applications, and for their use as super-compressive cushions, electrical contacts and switches, or thermal conduits, In this chapter, VACNT arrays will be tested under low cycle uniaxial compressive loading. Deformation variation of the VACNT arrays corresponding to the different compressive displacement and counterface material elastic modulus will be explored respectively.

2.1 VACNT Array Sample Preparation

Vertically Aligned Carbon NanoTube (VACNT) arrays are densely packed regions of CNTs grown with a metal catalyst on a substrate. The VACNTs can be thought of as a "brush" with thousands of carbon nanotubes acting as bristles. Vertically aligned MWCNTs (multi-walled carbon nanotubes) were grown into VACNT "forests" on a Si wafer using a three- temperature zone chemical vapor deposition (CVD) tube furnace [42]. A thin film of Al_2O_3 (thickness: 10 nm) and iron catalyst (thickness: 2 nm) were deposited using an electron-beam evaporator on a silicon substrate with 600 nm thickness of silicon oxide. The substrate was used in the presence of ethylene gas as the carbon feedstock at high temperature (950ºC) for 5 - 25 min to grow the

CNTs. The grown VACNT forests had heights of ~1.2-1.4mm and covered regions up to 1 cm^2 in area, and individual tubes are estimated to have diameters of ~14 nm [42]. The forest is attached via an adhesive to a second Si wafer that acts as a structural support, the process of which inverts the growth region of the CNTs (formerly in contact with the catalyst covered Si wafer) so that a flat, uniform surface is presented after release from a sacrificial layer. Samples for testing were prepared by using a blade to remove sections of the VACNT array. The contacting area of the resulting sample was kept nominally at 0.5 cm^2 and had heights of ~1 mm. Samples for low cycle compression of VACNT s group are from one piece of array, while samples for low cycle compression of VACNTs with different couterface stiffness are cut from another piece of array.

2.2 Contact Counterface Material

Two types of materials were used as the contact counterfaces when doing compression test: lithium niobate ($LiNbO_3$) and a gel polymer. Counterface materials are cut, using a stainless steel blade, into 1.5cm*1.5 cm (W*L) square pieces with thickness of ~1.5mm, which are large enough in area to guarantee VACNTs are fully in contact with the counterface when compressed. Ultrasonic cleaning in purified water was performed for 30 sec on each sample. Counterface materials are wax mounted to the loading anvil. Wax is utilized as an adhesive due to the strong adherence between the materials and the compression anvil, as well as the ease of removal of the samples from the anvils. If using a strong adhesive, the samples were found to become easily

damaged when removed from the sample holder.

Lithium Niobate

LiNbO$_3$ is a ferroelectric material of considerable interest to the optical, laser, and communications industry, due to its large values of nonlinear optical, electro-optic, piezoelectric, and acousto-optical coefficients [43]. Here, good surface finishing in terms of roughness and large surface stiffness are the reasons why it is chosen as the compression counterface. Since it is much stiffer than the VACNT array (LiNbO$_3$:202Gpa [44]; VACNT: 15-100MPa [26, 29]), and the surface roughness is on nanometer scale, the most significant strain energy when performing compression will be in the VACNT sample.

Gel Polymer

A polymer gel is used as a compliant counterface material. Its elastic modulus is 1Mpa [45] which 10-100 times smaller than VACNTs stiffness (15-100MPa [26, 29]), thus during compression with CNTs, the VACNT sample and also the gel counterface will deform. The idea of using soft material as one contact substrate is to find out whether contact counterfaces with different elastic modulus will cause changes to the compression results.

2.3 Fullam Loading Stage/Digital Microscope

The loading instrument used for the compression test is a displacement controlled precision stage (Fullam, Latham, NY). The apparatus is designed for high precision load or displacement controlled uniaxial tension or compression testing under light microscopes. Steel compression

anvils are fixed by screws to the stage. In this experiment, VACNT samples on silicon substrates are wax mounted to one compression anvil and the counterface is mounted to the other. The distance between two anvils can either be manually controlled or by the software setup. The load cell and displacement transducer have resolutions of +/- 0.5% of their full scales. The full displacement travel of the stage is 60mm and has a max strain rate of 9mm/min. The load cell has a range of 4.5kN (1000lb). When the experiment is running, the two anvils move towards each other (compression) or back from each other (relaxation). Displacement of the anvils and the applied load data corresponding to time are recorded during the test. After the test is finished, load-displacement curves can either be plotted in the software or the raw data can be copied as a text file for further analysis.

The precision loading stage is placed beneath a high-resolution digital microscope (Kenyence VHX-500) for real time imaging during the compression test. The digital microscope is composed of a camera, lens system, and a monitor with a built-in computer system for image processing and storage, and has 1600*1200 pixel resolutions for still images and an 800*480 actual pixel resolution for videos at a frame rate of 15F/s. A VH-Z100 zoom lens is used for the imaging which has a zoom capability up to 1000x [46].

2.4 Compression Test Setup

To observe in situ the buckling of the VACNT arrays, uniaxial compression testing was performed using the precision stage. The stage was mounted under the digital microscope for real time imaging (Fig. 2.1). The substrates which the CNT arrays are attached were mounted

with wax to the stage, with one end free.   Uniform compression is applied perpendicular to the array for prescribed displacements using the counterface substrates.

Low Cycle Compression of VACNTs

Arrays were compressed up to ten cycles, with each cycle involving an initial contact of the surface, a displacement to a prescribed value, and a retraction to an initial position.   Subsequent cycles began at the new surface location.   Before, during, and after each cycle, an optical image was taken from the side of the sample compressed region. The counterface used in the test was $LiNbO_3$ (described in 3.2), which has a surface roughness on the nanometer scale, and was chosen to provide a surface with much larger stiffness such that all deformation would occur in the CNTs.   The prescribed displacements (δ) used were 50 µm, 100 µm, and 200 µm, with a compression rate of 10 µm/sec and a retraction rate of 1 mm/sec.   Images were used to determine the extent of the CNT buckling region and the total height of the CNT array after each cycle.   Buckling was observed optically to occur only at the surface in contact with the substrate, and not throughout the bulk or at the location where the array was mounted with epoxy (Fig. 2.2) (Fig 1.1). Measurements for array heights and buckling region lengths were made across the entire width of the sample surface to obtain statistical significance in the results. Values were obtained for no less than 10 data points with the buckling region length defined as the distance from the free surface to the location where the first buckle met with the straight tubes in the array, and the total array height defined as the distance from the free surface to where the array was attached to the underlying substrate. （Fig.2.3）

10

Low Cycle Compression of VACNTs with Different Counterface Stiffness

Two types of counterface materials with an order different compliance were used for low cycle compression to observe effects on the VACNT buckling. The compression displacement (δ) is fixed to 100 µm for each cycle in this test. The two counterface materials used were $LiNbO_3$ and a gel polymer (see chapter 2.2 for material details).   Testing methodology proceeded in the same order as the previously explained compression test.   Images and measurement data of the buckling length and total array height before and after each loading cycle are defined and recorded.

2.5 Low Cycle Compression of VACNTs Test Results

The measured buckling region length and the total VACNT array height are plotted in Figs. 2.4 – 2.6.   Ten cycles were performed for each compression displacement except for the 200 µm case.   The total height of the array for δ= 200 µm decreased rapidly (see Fig. 2.6b) and a crushing of the forest (severe out of plane displacements) was observed when tests were performed beyond that, making further compression cycles inconsistent with the other data. Buckling period was observed by SEM to be 10 – 12 µm (Fig. 1.1) and consistent with other reports [44].   For each displacement value, the trend in the buckling length results had variations which were distinctly different. The δ= 50 µm compression test exhibited three regions associated with the buckling, beginning with an abrupt increase in the buckling length after the first cycle (Fig. 2.4a).   This represents the initiation or the first buckling length.   Subsequent

compression cycles manifested a decrease in buckling length after each cycle until the 7th. This region is associated with a compression of the initial buckling region within itself, and corresponds to the overall decrease of ~20 µm in the total array height (Fig. 2.4b). As the cycles continue, a constant value of the buckling length is reached of ~55 µm. For the δ= 100 µm case, there is a markedly different construct to the buckling length change with respect to compression cycles (Fig. 2.5a). Similar to the aforementioned δ= 50 µm case, the buckling length increases for the first cycle. A region spanning from the 2nd to 4th cycles shows an increase in the buckling length, indicating that the previous compression of the buckling zone does not occur, at least not immediately. A constant value of ~150 µm is observed after the 4th cycle, which is a region where further applied displacement is elastically absorbed by the buckling region and is evident in the total length remaining constant (Fig. 2.5b). Similar phenomena were observed in the high cycle compression tests by Cao et al. [1]. What is interesting is that the buckling length continues to increase while the total length decreases during the 10 cycles. This indicates for changes in applied displacement that different asymptotic values of the buckling length exist, and that the buckling region for the δ= 100 µm case is fully absorbing the displacement within the buckling region once a critical value was reached. There was some indication from observations that outside of the buckling region after the first few cycles, cracks would occur in the unbuckled regions close to the edge of the buckling region. After additional cycles, these cracks resulted in buckling which would extend the buckling region even though the substrate never came in contact with it. This is evidence of a fatigue in the CNT array, and shows the potential extent of it being ~50 µm beyond the

12

buckling region front. In the case of the largest displacement, δ= 200μm, which was subjected

to only three compressive cycles, a similar trend as for δ= 100μm is observed, but the rate of the

buckling length increase and the rate of the total array height decrease are much larger (Fig. 2.6)

indicating a further dependence on applied displacement. Asymptotic values for the buckling

and height are not observed with this case as were the two smaller displacements, due to the

array becoming crushed at increasingly higher displacements. This is different to results for

high strain (85% compression of the total height) seen previously [26], which were found to

rebound from the large compression displacements even after 1000 cycles. This could be due

to the differences in boundary conditions, where a fully released (unattached) CNT array film

was used in those studies.

2.6 Low Cycle Compression of VACNTs with Different Counterface Stiffness Test Results

Measurement of CNT array buckling length and normalized total array height （ratio of

current array height over the initial height） for each cycle was done for both groups (Gel as the

contact counterface & $LiNbO_3$ as the contact couterface). Results are plotted in Fig.2.7-Fig.2.9.

With respect to the normalized total array height variation, for Gel compressed sample, the array

height decreased less than 5% of the initial height with 10 cycles of loading, while for the

$LiNbO_3$ compressed sample, the array height is decreasing at a rate about 0.03/cycle and finally

reached ~0.67. The buckling length variation trend doesn't show too much difference between

the two counterface groups. Buckling length of the two both abruptly increased to values of

~118μm for the $LiNbO_3$ compressed case and 45μm for the Gel compressed case after the first

loading cycle which indicates the initiation of the buckling, and continue increasing for the 2nd cycle due to the spanning of the buckling region. It keeps on spanning till the 6th cycle although in a not very stable manner due to the complex structure change in the sample. With repeating cycles, it is slightly increasing but more likely reaching a steady state, 150μm for the $LiNbO_3$ compressed case and 130μm for the Gel compressed case. However, the absolute value of the buckling length of each cycle for the two cases have noticeable differences, which is mainly because the two samples went through different deformation evolution if looking back at variation trend of the normalized total array height as a reference. For the $LiNbO_3$ compressed case, buckling length is increasing with loading cycles but the total array height decreasing correspondingly can be explained as new buckling was forming causes the increasing of the buckling length for the first several cycles, but from the 6th cycle where a constant buckling length is reached, the buckling region is starting to be compressed causing dynamic equilibrium condition of the buckling length but the overall length of the array shows a decreasing trend. For Gel Polymer compressed case, the increasing buckling length is also due to new buckling formation but when a steady state was reached (6th cycle) the total array height remains constant which indicates that further applied displacement is elastically absorbed by the buckling region and the Gel Polymer counterface. Since $LiNbO_3$ is orders of magnitude stiffer than the VACNTs sample, the applied displacement can only go to the VACNTs array resulting in similar buckling region formation but more decreasing in total array height compared to Gel Polymer compressed sample. With the same amount of applied displacement to the two compression counterparts, $LiNbO_3$ compressed VACNTs absorbed entire strain energy but Gel Polymer compressed

14

VACNTs absorbed partially and the rest goes to the Gel Polymer. Thus, even though the buckling regions of the two have similar length, the intrinsic properties of them are expected to be different. Nanoindentations were performed in this region for both cases to explore the stiffness differences between the two, which is described in detail in Chapter 3.1.

2.7 Compressive Response Analysis

Measurements of the buckling region lengths after compression have found that the CNT array permanent deformation decreased with multiple cycles when displacement is small, however, with the increase of compression displacement, buckling lengths increased until reaching a critical value after only a few cycles. With a further increase in displacement the deformation becomes fully plastic, which causes the buckling length to continue increasing in an uncontrolled manner with the cycles.   This is better realized by considering the first three cycles of the buckling length variation (Fig. 2.9).   An intriguing result becomes evident when observing all three compression displacement results together, where for the first cycle, the buckling region lengths come to a similar value of ~70 µm, regardless of the applied displacement amplitude. Thus, the results seem to indicate that there is a critical length of permanent buckling that will occur after only one cycle.   This could occur due to the array only being capable of absorbing a specific amount of energy in the form of buckling for an undeformed sample. Once buckling is established, compression within the buckling could occur or further buckling may occur once a compaction limit is reached.   This is difficult to establish precedence with, since only one other study has performed cyclic actuation for constant

15

amplitude of the same samples [1], and no studies have measured the extent of the buckling

length region.   It is unknown if this critical value is inherent to densely packed CNT arrays, as

seems to be for the 10 – 12 µm periodicity in the CNT buckling, or if it is dependent on the

boundary conditions or the fabrication methods of the arrays.   For the studies reported here, all

CNT arrays were utilized from the same processing and handled in a similar manner, which has

lead to the repeatability of the data.   When observing the results in Fig. 2.9 after the first cycles,

it becomes evident that the initial permanent buckling serves as a demarcation point, and for

displacements below the value (i.e. 50 µm) compression of the buckling occurs, and for larger

displacements, an increase in buckling length occurs.   Additionally, a transition between

extensions of the CNT buckling length to a constant value with cycles versus uncontrolled

extension occurred above 100 µm.   The ceiling for this value is unknown and is presumably

linked to the applied strain and hence array height; though the independence of array modulus

with height has been demonstrated for strains similar to here (up to 0.2) [27], for single cycle

compression.

Another approach to the uniform compression results is to consider not only the applied

strain in the entire system, but the local strain which is occurring in the buckling region at the

surface.   Strains in this region will be indicative of the ability for the array to absorb energy and

be used in repeated contact applications.   The applied strain (ε_a) is defined from an initial array

state, where $\varepsilon_a = \delta / L_o$, though as the cycles are increased, ε_a will increase since δ will remain

constant for the displacement controlled compression and L_o will decrease after each cycle due to

the permanent array deformation.   If the local strain within the buckling region (ε_{local}) is defined

16

by,

$$\varepsilon_{local} = \frac{L_B - L_B^*}{L_B^*} \qquad (1)$$

where L_B is the buckling region length and L_B^* is defined through a constant initial array height L_o by,

$$L_o = L_B^* + L_U^* \qquad (2)$$

with L_U^* an initial unbuckled region length assumed to be approximated by $L_U^* \approx L_U$. The unbuckled region length is measured after each cycle as $L_U = L - L_B$, with L the total array height after each cycle. Eq. 1 can be rewritten using Eq. 2 and the assumption above as,

$$\varepsilon_{local} = \frac{L_B - (L_o - L_U)}{L_o - L_U} \qquad (3)$$

which provides a representation of the local strain in the buckling region. Eq. 3 only remains valid when the assumption of $L_U^* \approx L_U$ holds, which is not the case for all data acquired here. Fig. 2.10 shows the results of Eq. 3 versus compression cycles for the uniform displacements. The case of $\delta = 200$ μm is not plotted for comparison because the assumption for Eq. 3 does not hold since L_U falls in value for each cycle. Comparing the cases of $\delta = 50$ and 100 μm, the

17

results for the local compressive strain continue to increase with cycles for $\delta = 50$ μm, not

leveling off until the 7th or 8th cycle for values of -0.29 to -0.35.   This shows that the array

continued absorbing energy as permanent strain, with an increase in compaction of the buckling

region occurring with cycles.   It is fully believed that if the cycles were carried out for this

applied strain level, then a further leveling off of the local strain would occur.   For the higher

displacement of $\delta = 100$ μm, the results show that a constant value of ~ -0.1 is reached rapidly,

indicating that no significant plastic deformation of the buckling region is being added after each

cycle, and the displacement remains in a fully elastic regime.   The fact that the 100 μm case has

a smaller asymptotic local strain may be misleading, in actuality the overall buckling length for

this case is larger in value than the 50 μm case, though what Fig. 2.10 is presenting is the overall

strain within this buckling region with cycles.   Fig. 2.10 shows that the 100 μm case has a more

rapid rise to the asymptotic local strain value, as well as less overall compaction occurring with

$\varepsilon_{local} = -0.1$ versus ~ -0.3 for the 50 μm case.   For larger applied strains (beneath a critical limit,

as observed here the 200 μm case has uncontrolled buckling growth) the results give evidence

that compaction and growth of the buckling to a critical value is important for the response of

successive compression cycles.   Below a specific applied strain, the critical energy necessary

for the sustained steady-state energy absorption in not obtained, and further energy through

compressive cycles must be applied prior to a steady-state local value of strain being obtained.

Since the period of the buckling is observed to remain consistent, a critical length of the buckling

region is necessary to act as an energy absorbing cushion, or reorganization within the bulk of

the array may be occurring creating entanglements which provide elastic stiffening.   Further

18

study into the effects of the counterface surface conditions (i.e. roughness and surface energy) is of interest to determine the effects of the free surface boundary conditions on the buckling length and overall array compression. The results reported here are the first to show the transition for applied displacement affecting the evolution of the buckling region in VACNT arrays, and demonstrate that for changes in the applied strain from only 7.5% to 16%, compressive displacement can create an uncontrolled growth of the buckling region. It is shown that the buckling region is responsible for the absorption of the applied displacements when fixed arrays are repetitively compressed and can elucidate the applicability of the materials for applications, such as switches, MEMS devices, or surface cleaning, where oscillatory contact conditions will be important.
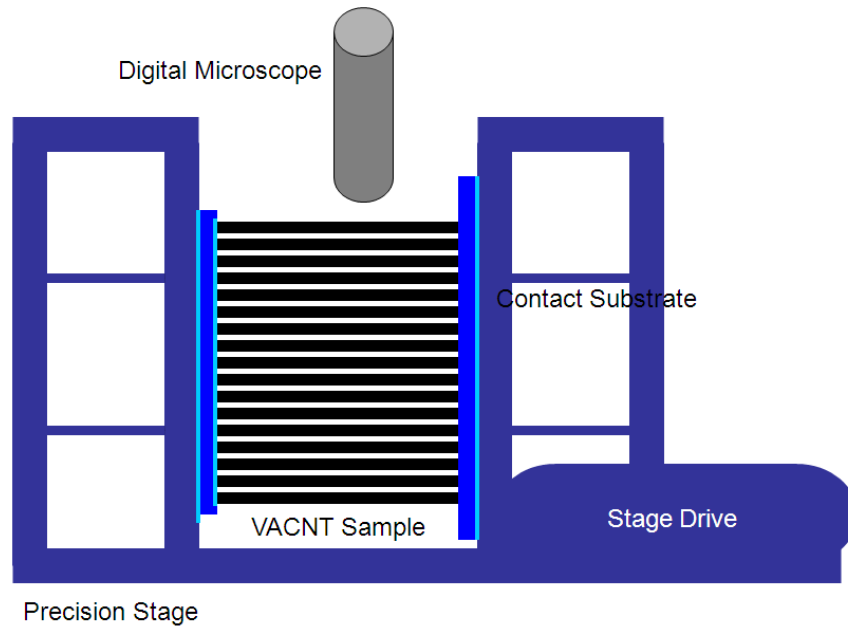
Fig. 2.1 - Testing apparatus showing the VACNT arrays mounted to the stage on the left side with a free surface towards the right of the figure; the contact substrate is attached to the right side of the stage; the digital microscope was positioned directly above the VACNT-LiNbO₃ contact interface to capture the compression and post-buckling region length.
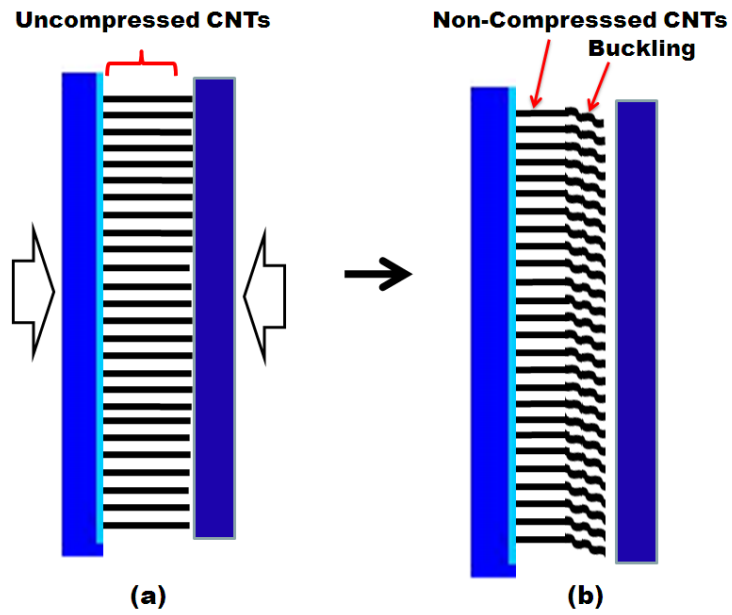
Fig. 2.2 - (A) Compression of the VACNT free surface, with the CNTs anchored at the bottom to a substrate; (B) Retraction from the VACNT surface reveals the buckling region that forms from contact with the contact substrate at the top surface.
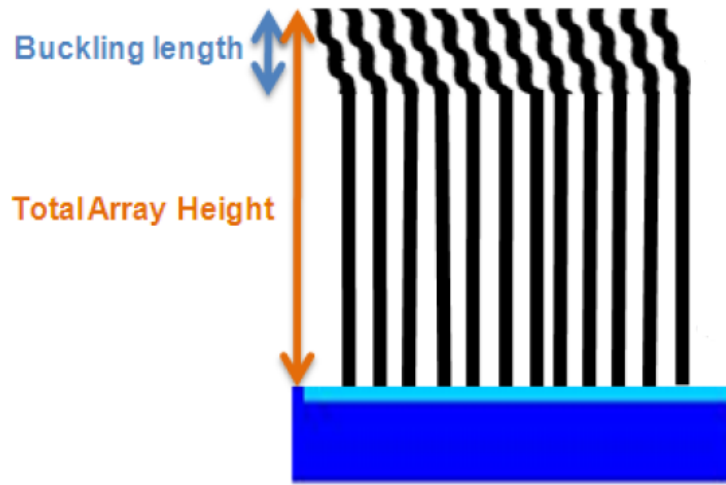
Figure 2.3 Buckling Length/Total Array Height Illustration

$\delta = 50$ μm

(a)

$\delta = 50$ μm

(b)
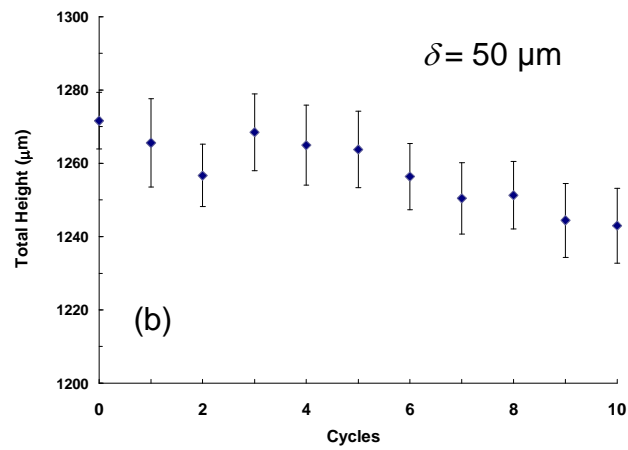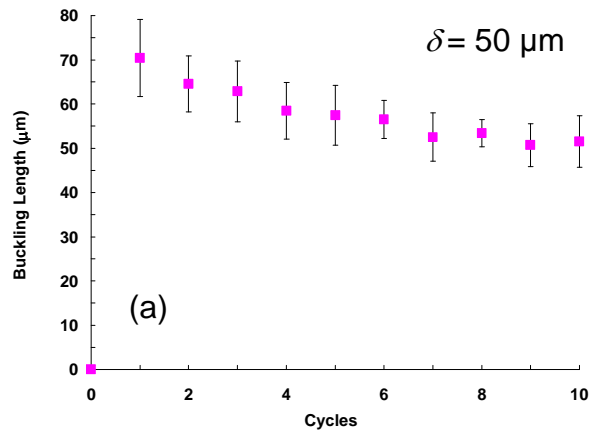
Fig. 2.4 - (A)   Buckling region length measurement as a function of compression cycles for the 50 µm displacement case; (B)   Total array height measurement as a function of compression cycles; Initial buckling length is compressed with increasing cycles reaching a steady-state value at ~7th cycle.
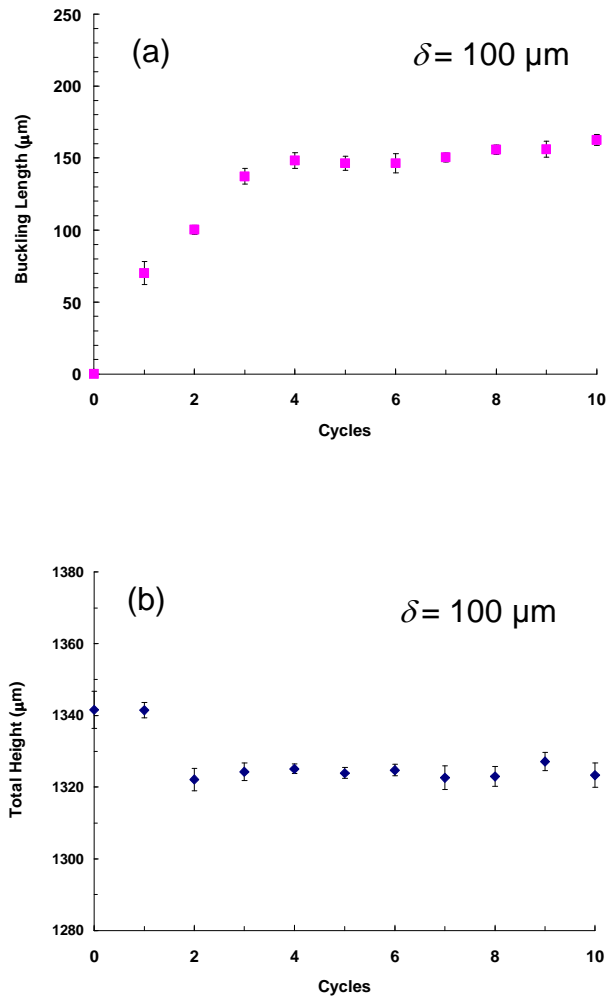
Fig. 2.5 - (A) Buckling region length measurement as a function of compression cycles for the 100 μm displacement case; (B) Total array height measurement as a function of compression cycles; Buckling length continues to grow with increasing cycles reaching a steady-state value at ~4th cycle.
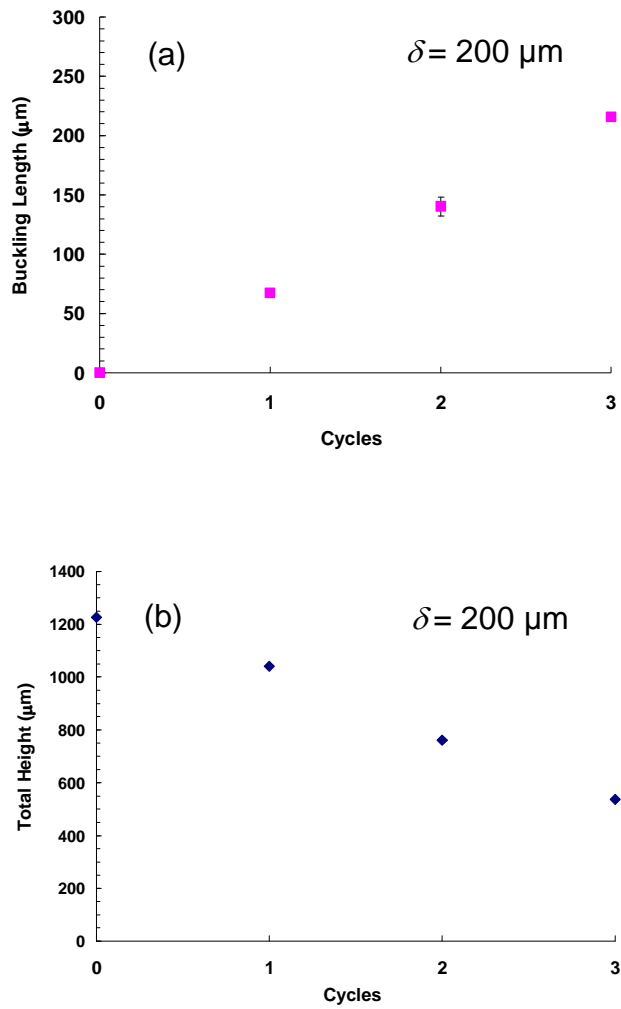
Fig. 2.6 - (A) Buckling region length measurement as a function of compression cycles for the 200 μm displacement case; (B) Total array height measurement as a function of compression cycles; Buckling length grows with increasing cycles, as the total height decreases.   Only 3 cycles were performed due to the severe height change.
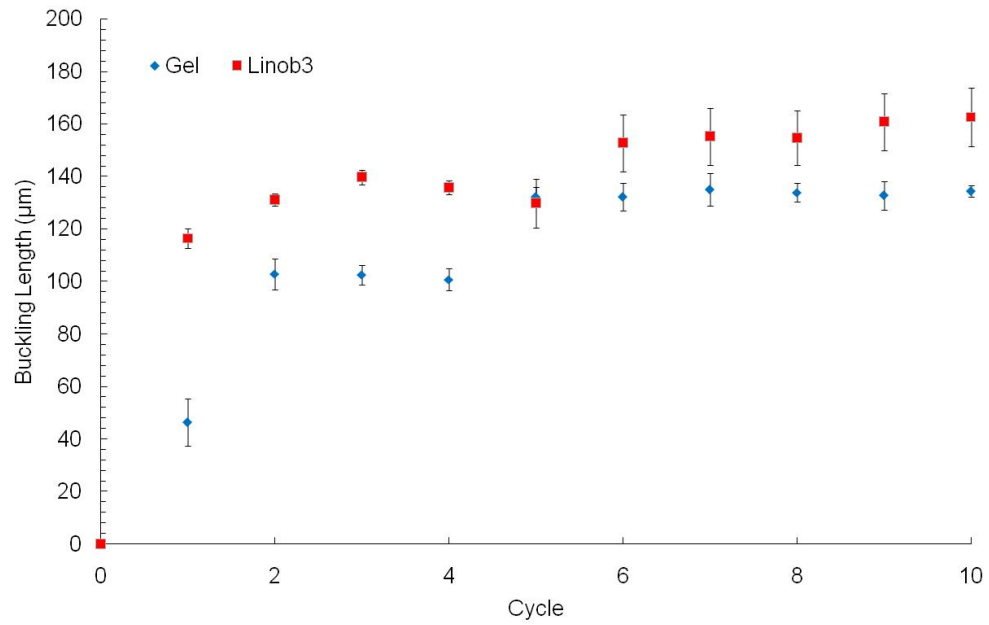
Fig.2.7- Buckling region length measurement as a function of compression cycles for 100 μm displacement on Gel versus LiNbO$_3$
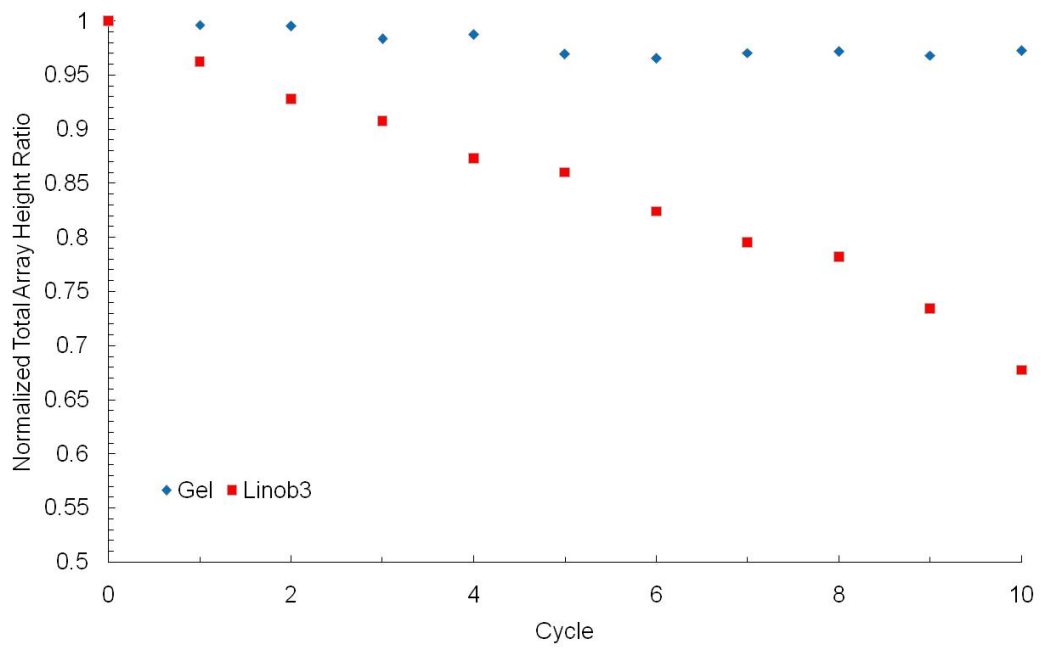
Fig. 2.8- Normalized total array length measurement as a function of compression cycles for 100 μm displacement on Gel versus LiNbO$_3$
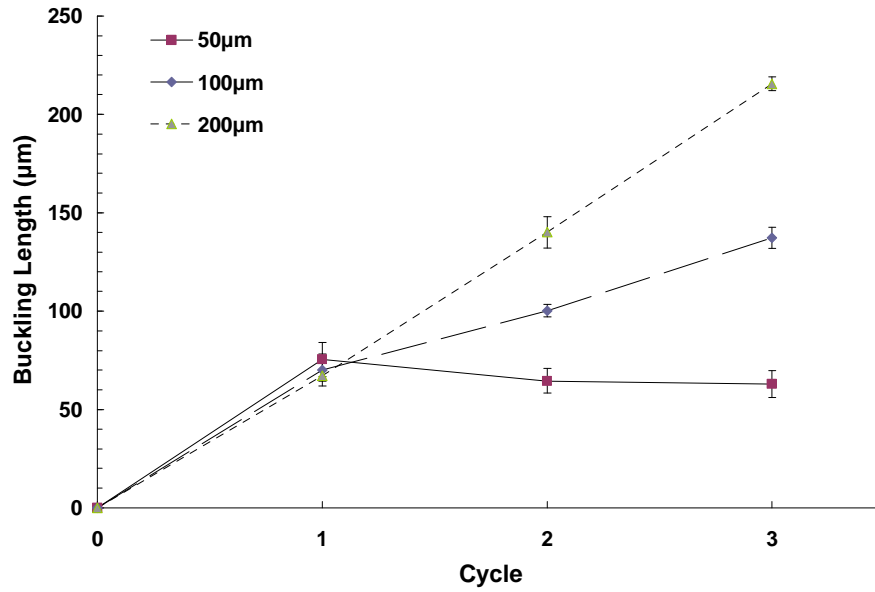
Fig. 2.9 - Measurements of the buckling length for the first three cycles of the three displacement cases. All cases have a similar buckling length after the first cycle, after which the 100 and 200 μm cases increase in length and the 50 μm case shows a small decrease.
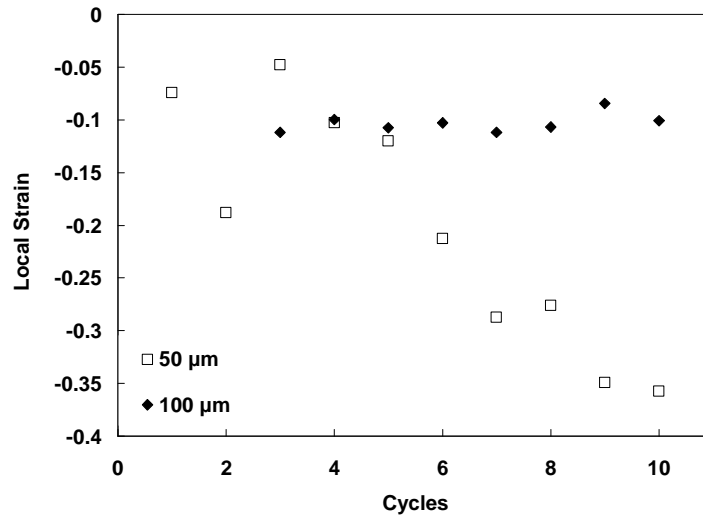
Fig. 2.10 – Local strain (Eq. 7) as a function of compression cycles for the δ = 50 and 100 μm cases. The 100 μm displacement reaches a steady-state earlier than the 50 μm case, where the strain remains inside the buckling region. For the 50 μm case the local strain increases with cycles due to compaction within the buckling region until reaching steady-state after the 7th cycle.

Chapter Three - Characterization of CNT Arrays by Nanoindentation and Raman Spectroscopy

Low cycle compression will result in localized buckling occurred to the VACNT array. The intrinsic property of the buckled region, which acts to provide energy absorption when using VACNT array to compression applications, is of great interests and importance. In this chapter, the buckled and unbuckled regions of samples tested in Chapter Two will be characterized and compared using Nanoindentation and Raman Spectroscopy techniques, which will provide elastic modulus and the vibrational characteristics of the tested regions respectively.

3.1 Characterization of CNT Arrays by Nanoindentation

Instrumented Indentation

Nanomechanical property testing of the VACNT was performed using an instrumented indenter (MicroMaterials NanoTest) to obtain Young's modulus of the VACNT arrays. During the indentation process the apparatus measures the movement of the indenter in contact with the testing sample and the displacement and load applied during loading/unloading are recorded. The instrument has a resolution of $0.2\mu N$ for the load and $0.06nm$ for the depth.

Microscale compression of the VACNT arrays was performed using the instrumented indenter with a large radius (5 µm) of curvature diamond indenter. Sample substrates were mounted using wax to create a strong bond to the aluminum sample stub and allowing easy removal. Indentation tests were performed before and after the uniform compression tests. Five load-controlled indentations were made on each sample surface with a loading and unloading rate of 0.01 mN/s. Indentations were spatially placed across the surface to maintain an accurate representation of the near-surface properties. The load-displacement curves were utilized to determine the slopes of the initial loading and unloading portions of indentations, and to calculate the elastic modulus of the VACNT surfaces. Five different VACNT array samples were nano-indented following the above procedures: 1. An uncompressed sample; 2. A sample after 10 uniaxial compressive loading/unlodaing cycles with displacement δ=50µm. 3. A sample after 10 uniaxial compressive loading/unloading cycles with displacement δ=200µm. 4. A sample after 10 uniaxial compressive loading/unloading cycles with displacement δ=100µm. (Note: they were all compressed to $LiNbO_3$ substrate). 5. A sample after 10 uniaxial compressive loading/unloading cycles with displacement δ=100µm but the contact substrate was changed to Gel Polymer. (Note: The compressive responses of all these five samples were discussed in Chapter 2)

The elastic stiffness of all 5 samples is analyzed by performing a linear regression of the first 500 nm of the unloading data similar to Doerner and Nix [47], after the maximum displacement value began to decrease, to obtain a slope, S ($= P / h$), where P is the applied load and h is the measured displacements. This was performed for each unloading curve and

31

averaged.   The slope of the unloading curve for spherical analysis can be related to the modulus of the CNT array through the reduced elastic modulus (E_r), using the Hertzian contact analysis radius [48],

$$a = \sqrt[3]{\frac{3PR}{4E_r}} \qquad (1)$$

and the mutual approach of the contact surfaces $h = (a^2 / R)$, where R is the indenter radius. The reduced modulus is,

$$\frac{1}{E_r} = \frac{1 - v_s^2}{E_s} + \frac{1 - v_i^2}{E_i} \qquad (2)$$

with E_i and v_i the elastic modulus and Poisson ratio for the diamond indenter equal to 1141 GPa and 0.07, respectively, and E_s and v_s the VACNT elastic modulus and Poisson ratio.   The exact value of v_s has been reported between 0 (foam-like material) to 0.19 (single nanotube), or alternatively the reduced modulus is simply reported by some authors, avoiding the CNT array Poisson ratio.   Using the geometric relationship for the apparent radius of contact as a function of the penetration depth (h_p) for a spherical indenter geometry,

$$a = \sqrt{2Rh_p - h_p^2} \qquad (3)$$

where hp is assumed to be the average of the maximum and residual indentations, and Eq. 1, the reduced modulus is written as,

$$E_r = \frac{3}{4} \frac{S}{\left(2Rh_p - h_p^2\right)^{1/2}} . \qquad (4)$$

Nanoindentation on Compressed VACNT Array Results

The Load versus displacement data acquired during the indentation are presented in Figs. 3.1– 3.5. All curves have a familiar form where indentation depth increases with applied load during loading. Once a maximum prescribed value is achieved, the load decreases as the indenter is retracted. These results in the unloading curve follow a different path, with load rapidly decreasing over a smaller displacement, and occur due to fully elastic retraction, versus the elastic-plastic loading curve. For all curves recorded, a residual indentation depth was observed when the indenter was fully unloaded. The residual plastic deformation of the CNT array is similar to the observed plastic deformation in the uniform compression tests, though it is not clear if this is due to the same buckling mechanism, since indentations are shallow enough to be within the critical buckling period of 10 – 12 µm. Though, compared to the results for the δ= 50 µm uniform compression test, it may not be necessary for a prescribed displacement to be of the same magnitude as a buckling region for formation, since the buckling region showed growth beyond the 50 µm displacement. Regardless, performing indentation at depths on the order of the buckling allows a clearer picture of potential mechanisms. From inspection of the

curves Fig3.1-Fig3.3 which are from low cycle compression of VACNT arrays(Chapter 2.5) (sample 1-3 defined in 3.1), two observations can be made of the results.   From the loading curves it is observed that at initial loading there exists a region of increased stiffness for the compressed samples extending up to ~500 nm, which is not present in the uncompressed samples. This is analyzed by measuring the linear slopes from a regression analysis of the loading curves for the first 500 nm of displacement (Fig. 3.6), and shows a ~17% increase between the compressed and uncompressed samples averaged over the indentation results.   After the first 500 nm, the loading curves take on a shallower slope which is approximately maintained to the maximum load.   Similar observations of an initial stiffening region have been observed by indentation with a blunted Berkovich diamond into VACNT array surfaces [30], as well as indentation into thin (200 nm to 1.4 μm) CNT array films [31].   This event, best described as a knee in the loading curve, may occur due to tube buckling at the scale of the indenter, though since the knee was not observed in the uncompressed sample, which should undergo similar buckling, the stiffening may be due to a change in fiber orientations due to the permanent bending (from the buckling region) and an increased fiber entanglement.   Agglomerates of CNT aggregates have shown a similar behavior with an increase in stiffness occurring due to entanglements between microaggregates [25].   The second observation is a change in the slope of the unloading curves for the different samples.   The two compressed cases showed an increase over the uncompressed case in slope during unloading, indicating a larger elastic stiffness of the VACNT array.

For indentation results of low cycle compression of VACNT arrays with different contact

counterface   (sample 4 and 5 defined in 3.1), which Fig 3.4 & Fig 3.5 show, differences of both

loading and unloading curves can be seen between $LiNbO_3$ and Gel Polymer compressed cases.

$LiNbO_3$ compressed curve has stiffer slopes of both loading and unloading curves than the Gel

Polymer compressed case which is analyzed by taking linear regression of first 500nm

displacement of loading and unloading curves respectively. The stiffer slope of $LiNbO_3$

compressed case in terms of the loading curves indicates that with same indentation depth, more

force is needed for the indenter to penetrate through the sample than the Gel Polymer

compressed case.   By analyzing the unloading slope of the two, the $LiNbO_3$ compressed case

has a larger elastic stiffness of the array than the Gel Polymer compressed one.

The reduced modulus of the contacts was calculated using Eq. 4 for each case and averaged,

yielding results: sample 1-3: for the uncompressed samples of 13.2 +/- 0.3 MPa and for the

compressed samples of 14.4 +/- 2.4 MPa and 15.4 +/- 1.1 MPa (δ= 50 and 200 μm, respectively)

which shows a stiffened elastic unloading response for the compressed samples; sample 4 and 5:

for the $LiNbO_3$ compressed sample of 25.32+/-5.74 MPa and for the Gel Polymer compressed

sample of 12.19+/-1.16 MPa. The array modulus is approximated by the reduced modulus for v_s

= 0, since the array stiffness is small compared with the diamond indenter.   When a non-zero

value of the array Poisson ratio is chosen (e.g. v_s = 0.19), the array modulus follows the same

trend and is computed to be sample 1-3: 12.7 +/- 0.3 MPa for the uncompressed samples and

13.9 +/- 2.4 MPa and 14.8 +/- 1.0 MPa for the compressed samples (δ= 50 μm and 200 μm,

respectively); sample 4 and 5: 19.42+/-4.33 for the $LiNbO_3$ compressed sample and 9.24+/-0.87

for the Gel Polymer compressed sample. The magnitude of the values measured for the reduced

elastic modulus are similar to those reported by others, ranging from 15 – 100 MPa [26,29], though are lower than those reported for dense CNT films, which were 1-2 orders of magnitude higher [31].

The result for the increase in modulus observed for the uniformly compressed arrays (especially δ= 200 µm) may be due to the fiber interactions which hold the fibers in the buckled formation. Van der Waals interfacial forces present between neighboring nanotubes contribute to the buckling phenomena as well as provide an increased resistance when compressed at the scale of the individual buckle (the scale of the indentation measurements). When the nanotubes are in an initial state in the array, they are presumed to be approximately vertical; here the interfacial forces will be acting predominately perpendicular to the plane of the surface (normal to the tube surfaces). Once the nanotubes are in a permanently buckled state, due to the curved CNT surface, there will now be interfacial forces that act in the direction normal to the indentation surface. These forces may provide a resistance to the indenter unloading as the buckles relax, and this mechanism may also contribute to the increase in stiffness observed in the first 500 nm of the loading curves.

The higher elastic modulus of $LiNbO_3$ compressed arrays over Gel Polymer compressed arrays maybe due to more interactions between nanotubes since harder material compressed sample absorbed more strain energy which dissipated into the array resulting in more failure of nanotubes. Increasing of tube-tube interactions will provided more interfacial forces make the penetration and retraction of the indenter harder.

3.2 Characterization of CNT Arrays by Raman Spectroscopy

Raman Spectroscopy

Raman spectroscopy was performed to investigate the vibrational characteristic of VACNT arrays under strain.   Raman spectroscopy uses a laser to excite the atomic bonds in a material. A detector collects the reflected light and a comparison between the collected and original wavelengths gives information on the phonon modes in the system.   The Raman spectrum of a VACNT array which is mainly composed of MWCNTs is rich in information. For MWCNT, the most typical prominent Raman features of MWCNT are: the D-Band (disordered) and G-band (graphite) modes. The D-Band mode is a longitudinal optical phonon and is known as the disordered or defect mode because a defect is required to elastically scatter in order for the process to conserve momentum, this mode is usually located between 1300-1400cm^{-1} [36]; However, the presence of D-Band cannot be correlated to the presence of various defects (such as hetero-atoms, vacancies, heptagon-pentagon pairs, kinks, or even the presence of impurities, etc) [36].   Usually, the D-Band feature is utilized by combining with G-Band feature. The intensity ratio of the D-band peak over the G-band peak I_D/I_G is interpreted as the quality measure of nanotubes. The higher the I_D/I_G ratio, the more broken of the sp^2 symmetry of the nanotube happens [40], which in other words means more damage to the tube structure. The G-Band mode is a tangential shear mode of carbon atoms that corresponds to the stretching mode in the graphite plane and always located around 1580 cm^{-1}[79]. Since the G-Band is representing the stretching of the C-C bond, when the bond lengths and angles of graphene are modifie by strain, the hexagonal symmetry of graphene is broken [38]. Thus, G-Band is a very good

indicator of strain effects on CNTs, although G-band dependence on externally induced strain is still controversial [38]. SWCNT usually shows multiple G-band peaks due to the phonon wave vector confinement along the SWCNT circumferential direction and due to symmetry breaking effects associate with SWCNT curvature [35]. Nevertheless, MWCNTs mostly don't show obvious splitting of G-band or it is small and smeared out because of the effect of the diameter distribution within the individual MWCNT and because of the variation between different tubes in ensemble of MWCNT in typical experimental samples [35]. Thus, in most cases only a single G-band peak is observable for MWCNTs. However, for MWCNTs that contains very small diameter innermost tubes, it is possible to observe splitting of G-band because of the well-protection of the innermost tube by the outer cylinder and more significantly, the special small diameter (<2nm) nature of the innermost tube [50]. Also, those MWCNT always show RBM in the spectra which is supposed to be too small to be observed in MWCNT [35]. RBM is associated with the symmetric movement of carbon atoms in the radial direction and it is a measure of tube diameters. However, because of large diameter nature of most MWCNT, the RBM signal is too weak to be observable in most cases.

Raman spectroscopy performed here uses a Thermo Nicolet Almega spectrometer with a 758nm wavelength laser at 20-30 mW depending on the scanned region. 256 scans were taken over a 3600 cm^{-1}Raman shift. A measurement spot size of 1μm was used for the micro-Raman spectroscopy. Unbuckled and buckled regions were scanned on a compressed CNT sample that exhibited wave-like buckling patterns. Four ~5μm spatially resolved micro-Raman spectroscopy was obtained in the buckling and unbuckled region respectively.

Raman Spectroscopy Results and Analysis

The Raman spectra with frequency ranging from 1100-1700 cm^{-1} of both unbuckled and buckling regions can be seen in Fig3.7 and Fig3.8. For each spectrum, D-band (~1300cm^{-1}) and G-band (~1600cm-1) are obviously presented. The frequency and intensity values of each peak are picked up for analysis.   By averaging G-band peak values for spectra of both unbuckled and buckling regions separately, the average G-band peak value up shifted from 1602.2 to 1606.9 cm^{-1}. The average I_D/I_G ratio is calculated to be 1.40 for the unbuckled region and 1.44 for the buckling region. The 4.7 cm^{-1} Raman up shift of G-Band peak between unbuckled and buckling region indicates C-C bond change in the nanotubes, which can either due to the nanotue-nanotube interactions or due to the broken of sp^2 symmetry within the individual nanotubes. Rajay, etc [40] confirmed that when applying strain to the CNTs bundle, only a small fraction can be transferred to individual nanotubes within the bundle and most part of it will result in nanotube-nanotube interactions. Based on the very tiny I_D/I_G ratio change (~2.8%) between the strained region and unstrained region, sp^2 symmetry of individual nanotubes were not damaged, at least not affected much. Nanotube-nanotube interactions accounts mostly for the up shift of G-Band peaks. In the buckling region, compressive strain causes more interactions and bundle effect between nanotubes, which may further results in the abbreviation of the C-C bond reflected by the increase of the G-Band peak. The G-Band shoulder at lower frequency (~1577cm^{-1}) for both unbuckled and buckling region (Fig 3.7 & Fig 3.8) might be the splitting G- peak, which is common in SWCNTs but usually not observable for MWCNTs or it may be

due to defective graphite-like materials in the array [49].   No literature about G-Band splitting for MWCNT array was found so far. Further exploration of the G-Band shoulder is needed. At lower frequency regions of the Raman spectra, radial breathing mode (RBM) is observable for both unbuckled and buckling region arrays. Fig 3.9 shows two representative spectra of each case. Multiple peaks are presented, which may be due to that not only one nanotube contributes to the RBM because of the array effect and the multi-wall nature of MWCNTs. Here, a peak with highest intensity in the RBM region was chosen for analysis. The RBM frequency (ω_{RBM}) for the unbuckled region nanotube is 230.2 cm^{-1}, implying a diameter (d_t) of 1.03nm by the relation

$$\omega_{RBM} = A/d_t + B \hspace{3cm} (5)$$

where A= 223.5 cm^{-1} nm and B= 12.5 cm^{-1} [51]; for the buckling region nanotube, a diameter (d_t) of 1.05 nm was calculated from the RBM frequency of 224.9 cm^{-1} using equation (1). The small innermost nanotube diameter feature of the array sample may contribute to the shoulder of the G-band [50]. The 6.7 cm^{-1} down shift in the RBM frequency between the unbuckled and buckling nanotubes may corroborate the strain-induced debundling/bundlinig phenomenon [40]. More interactions and bundle effect in the buckling region are represented not only by the increase of G-Band frequency but also by the down shift of the RBM.

Another set of Raman scans (5 spots) with a spatial distance of 5μm in line was performed within the buckled region in order to explore its intrinsic Raman feature. The G-band peak versus the scan locations for each spot was plotted in Fig 3.10. The plot indicates that the G-band peaks

of different locations even within the buckled region have an approximately 1 to 7 cm^{-1} frequency variations. One possibility is that since the CNT is bent to failure, the C-C bond of regions along the nanotue might be elongated, abbreviated or remained. Thus, Raman scans in different locations along the tube growing direction might show variability in the C-C bond change reflected by the G-band peak shift. The other possibility is that there might be density or nanotube-nanotube interactions variations within the buckled region, which will cause different C-C bond change of CNTs. Although further exploration on the G-band frequency of different locations in the buckled region is needed, Raman feature variations occur not only between buckled and unbuckled CNTs but also within the buckling regions.
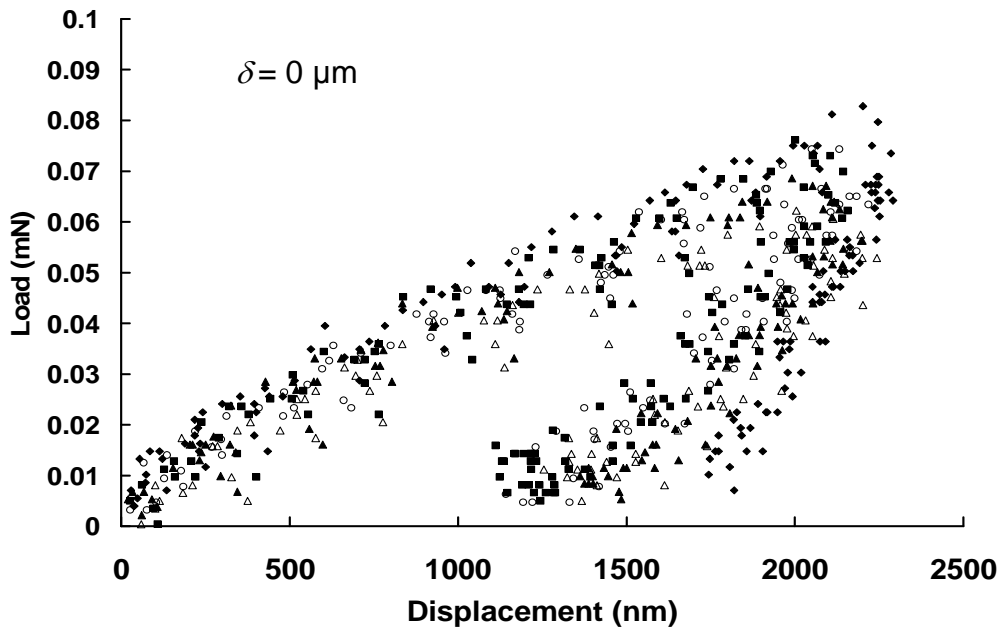
Fig. 3.1 - Load-Displacement curves from nanoindentation of uncompressed VACNT array.
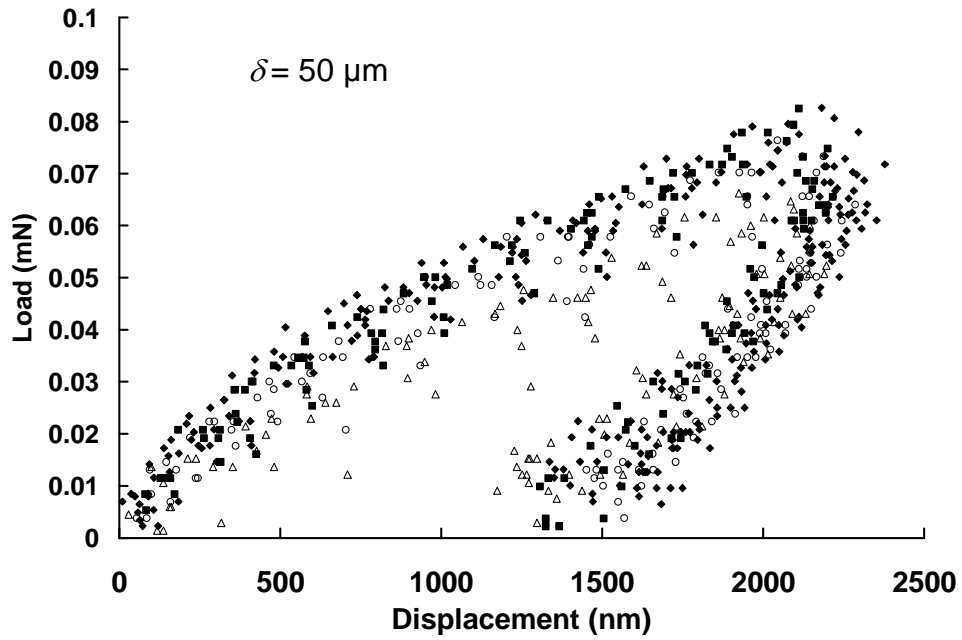
Fig. 3.2 - Load-Displacement curves from nanoindentation of compressed VACNT array after 10 cycles with δ= 50µm. Slope change in the loading curve is observed for the first ~500 nm.
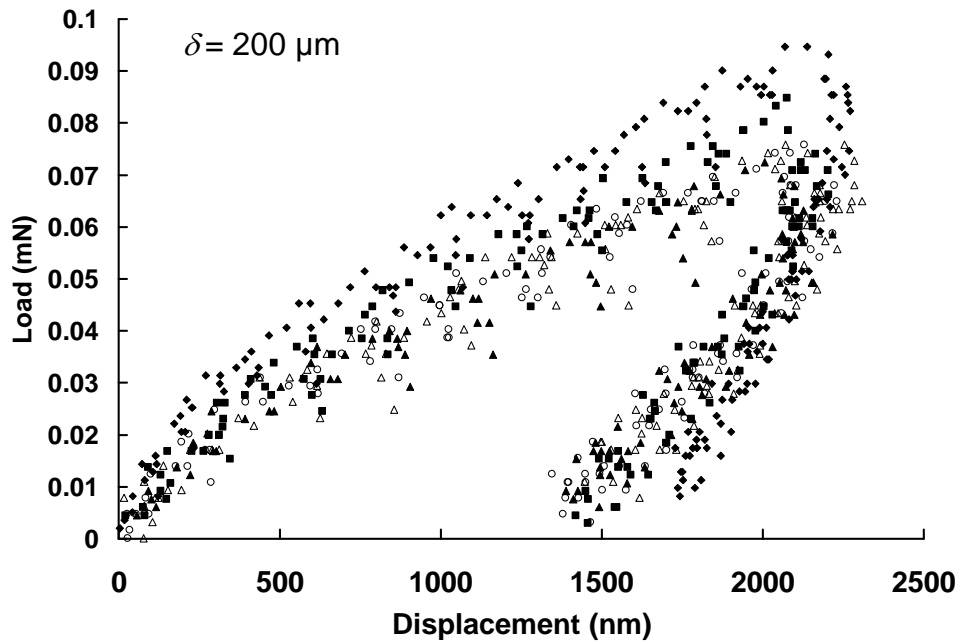
Fig. 3.3 - Load-Displacement curves from nanoindentation of compressed VACNT array after three cycles with δ= 200μm. Slope change in the loading curve is observed for the first ~500 nm. Increase in unloading slope is present compared with the uncompressed case (Fig. 3.6).
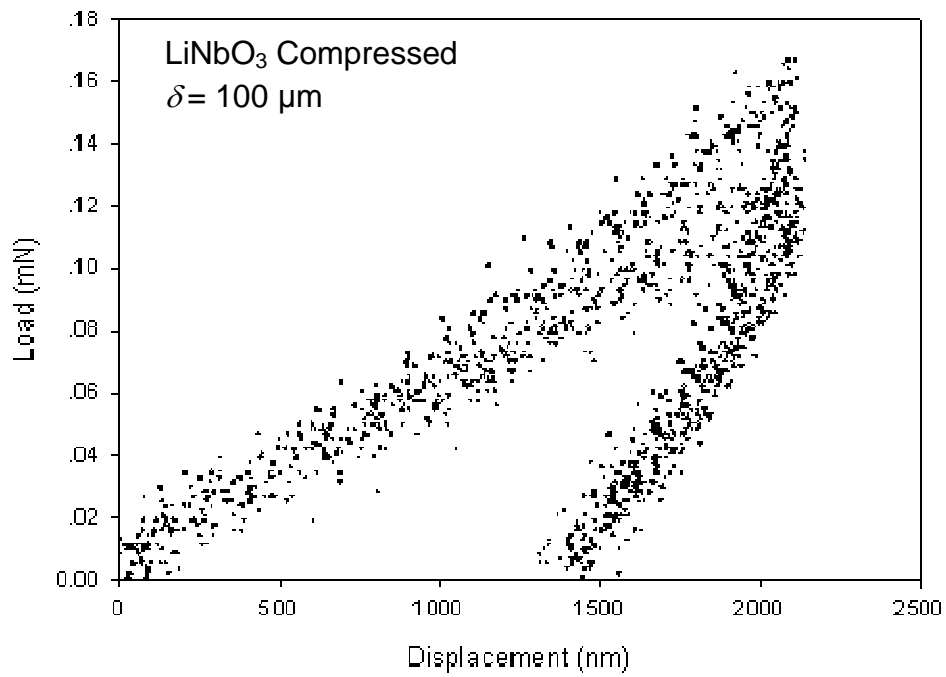
Fig. 3.4 Load-Displacement curves from nanoindentation of LiNbO$_3$ compressed VACNT array after ten cycles with δ= 100µm
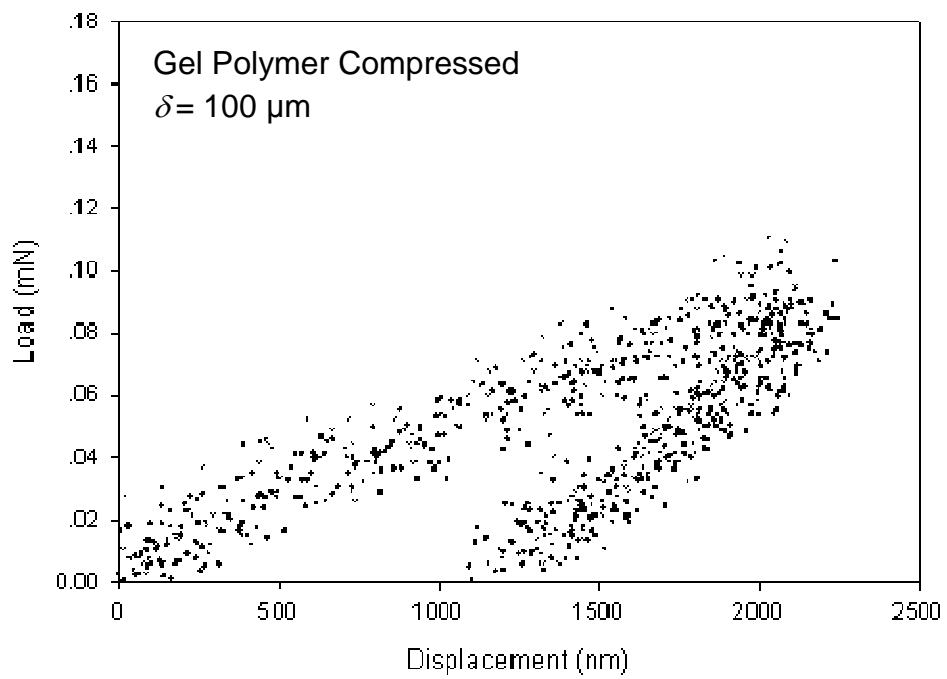
Fig. 3.5 Load-Displacement curves from nanoindentation of Gel Polymer compressed VACNT array after ten cycles with δ = 100μm
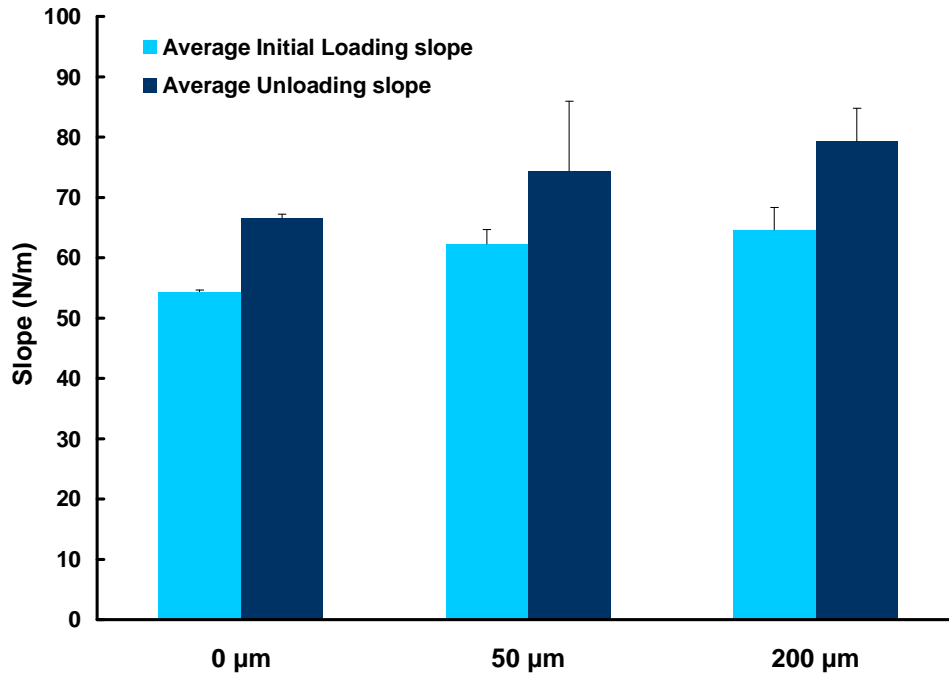
Fig.3.6 – Calculated slopes (N/m) by regression analysis of the initial loading (first 500 nm) and the unloading curves for indentations presented in Figs. 3.1-3.3. Increase in slopes is observed from the uncompressed state to the array compressed with 200 μm displacement.
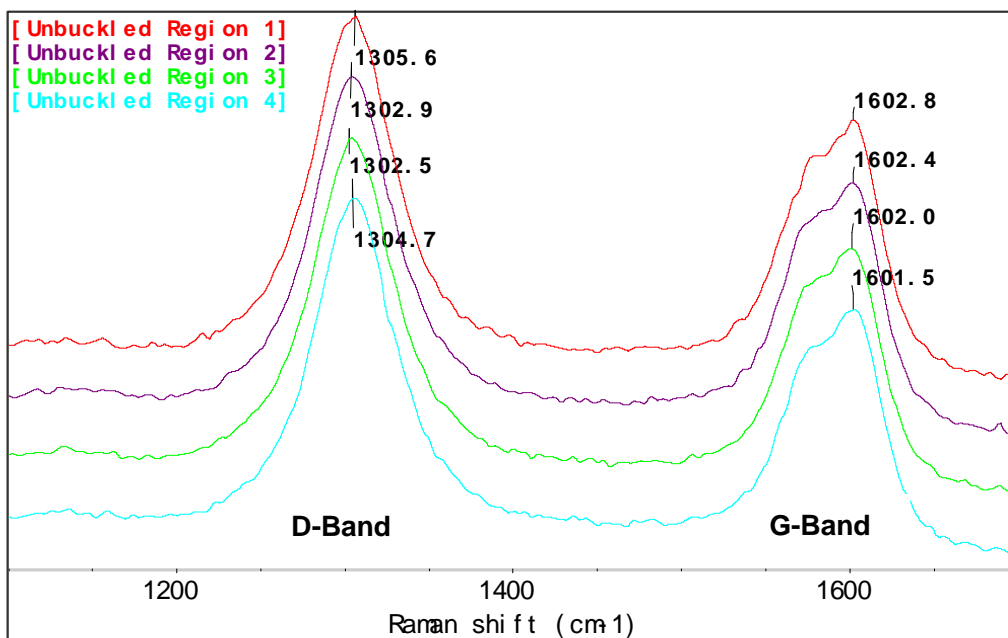
Fig.3.7 – D-Band and G-Band spectra in the uncompressed regions of the VACNT Array. Four scans were taken in line parallel to the nanotube growing direction and there is a 5μm distance between each scan spot.
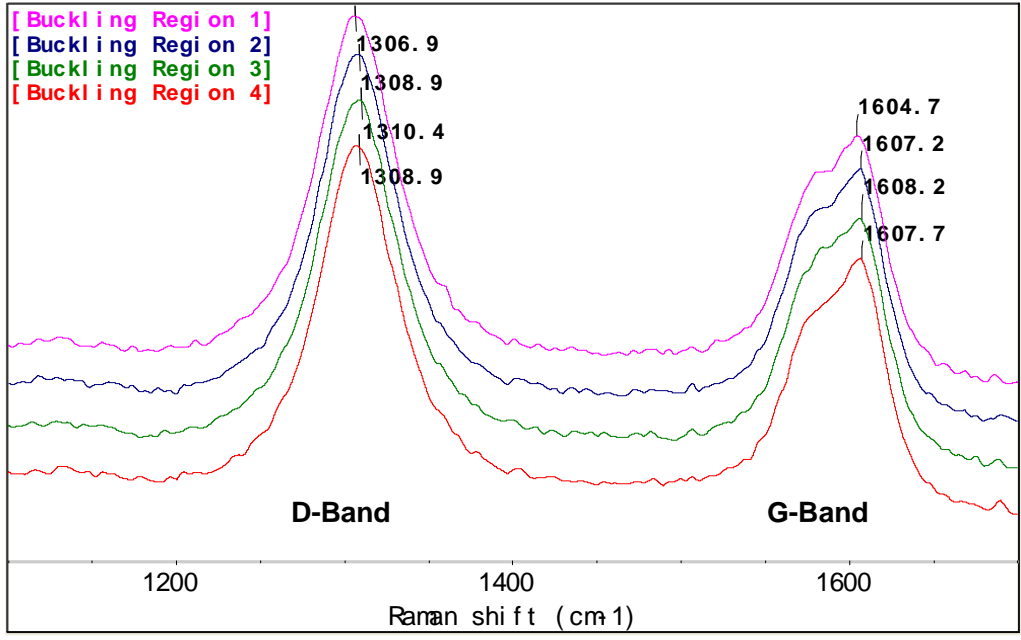
Fig. 3.8 – D-Band and G-Band spectra in the compressed regions of VACNT Array. Four scans were taken in line parallel to the nanotube growing direction and there is a 5μm distance between each scan spot.
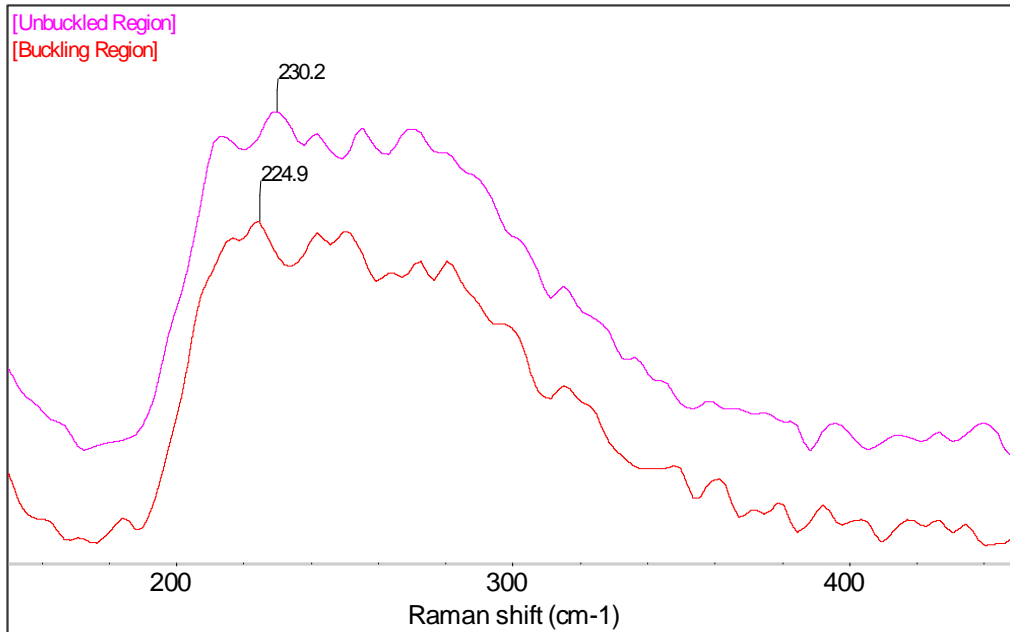
Fig. 3.9 – Radial Breathing Mode （RBM） comparison between unbuckled and buckled regions. The RBM peak down shifted from 230.2 to 224.9 cm^{-1}, which indicates a strain-induced bundling effect in the buckled region.
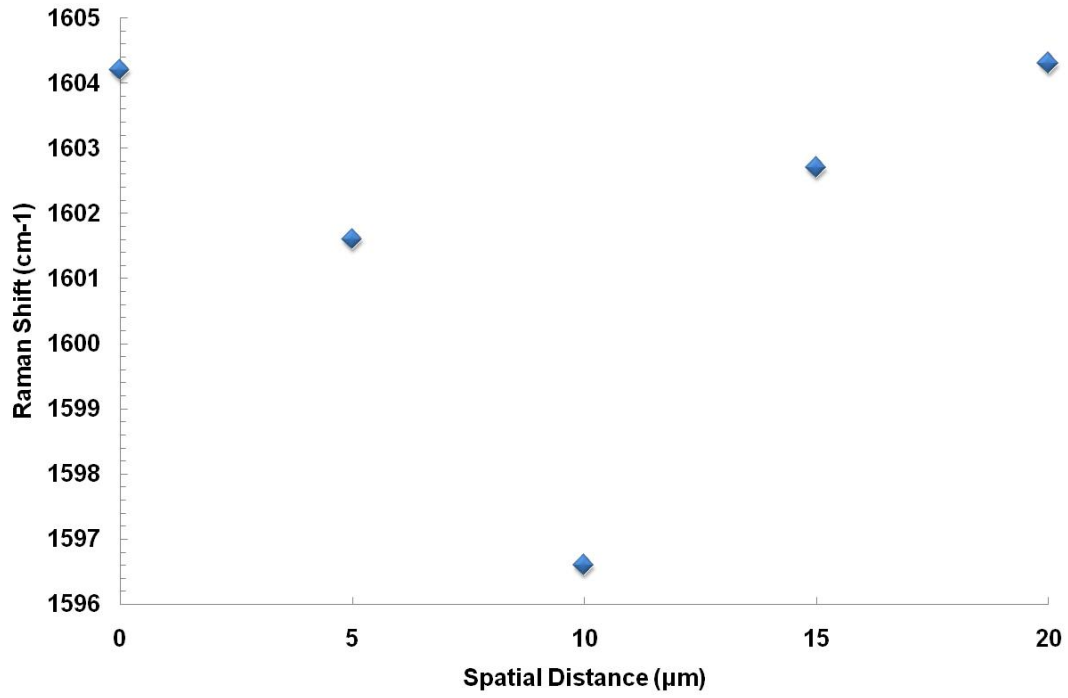
Fig 3.10 –G-Band Raman Shift (frequency) of different scan spots with a 5μm spatial distance in the buckled region

Chapter Four - Electrical Resistance Measurement of VACNT Array Under Compression

In order to use VACNT arrays for sensing applications, the electrical resistance variation of the arrays both in perpendicular and horizontal to the array growing directions under compressive strain is explored in this chapter.

4.1 Sample Preparation

Two types of CNT array samples were prepared for the test to measure resistance changes during normal compression; one, where resistance is measured perpendicular to the tube growth direction (lateral measurement orientation), and another type for measurement parallel to the tube growth direction (vertical measurement orientation).

Lateral sample preparation

A 5.55 x 4.35 x 3.33mm (W x L x H) MWCNT array grown on a Si substrate is used as the sample. The array is attached via epoxy gel, which is an electrically insulated adhesive, to a second Si wafer that acts as a structural support, the process of which inverts the growth region

of the CNTs (formerly in contact with the catalyst covered Si wafer) so that a flat, uniform surface is presented after release from a sacrificial layer. Two electrical leads with diameter of ~0.3mm were attached to the parallel vertical sides of the array via silver epoxy that has an electrical resistivity of 0.38 Ω-cm. The silver epoxy covered the entire span perpendicular to tube growth direction but with a thickness less than 20% of the array height on each side (Fig 4.1). The silver epoxy provides an adhesive for the wire electrodes and electrical conductivity between the electrode and the CNT array.

Vertical sample preparation

A 3.04 x 2.77 x 1.18mm (*W x L x H*) MWCNT array was used to prepare the vertical sample. The array was released off the growth substrate using a razor blade, yielding a freestanding structure. Two 0.25 mm thick copper plates coated with a ~70μm thick silver epoxy layer, deposited by spin-coating at a rate of 5000rpm for 60s, were attached to the two free surfaces of the CNT array forming a sandwich sample.   Two electrical leads were soldered to the copper electrodes (Fig 4.2).

4.2 Dynamic Resistance Measurements during Compression Testing

Electrical resistance change of the two samples prepared will be measured during low cycle compression test.

CNT Resistance Measurement Circuit

An electrical circuit was built in order to measure the dynamic resistance of the CNT array (Fig.4.3). The circuit is comprised of a 3 volt DC power supply, a 100 Ω safety resistor to avoid an open circuit, a 50mV/10A shunt resistor used to determine the current in the circuit, the CNT array and two signal amplifiers built parallel to the shunt resistor and the CNT array separately in order to magnify the voltage signals due to the small resistance of the two for measuring purpose and also in order to avoid applying high voltage across the CNT array. The output voltage signals from the amplifiers are transferred to a Data Acquisition System for real-time signal recording. The gain factors of the amplifiers built across the shunt resistor and the CNT array were chosen to be 1659 and 9 respectively so that the voltage signals can be magnified to values within the DAS resolution range. Since the shunt resistor has a known resistance (R_s), once the voltage (V_s) across it was obtained, the current (I) in this series circuit can be calculated by dividing the voltage by its resistance. The DAS provides the amplified voltage drop across the shunt resistor (V_s') and across CNT array (V_c') individually. The actual voltages of the two can be calculated by dividing the amplified voltage by the gain factors of the amplifiers across them respectively. The resistance (R_c) of the CNT array can be calculated by $R_c = V_c/I$. All the voltage signals corresponding to time before and during the compression test are obtained by the DAS with a sampling frequency of 30Hz. Resistances of the CNT arrays after each loading cycle were calculated using the method described above for each data point from DAS and then averaged. Current strain was calculated using the measured array height values by dividing the change of array height after each loading cycle by the array height value before the current compression

54

cycle.

Lateral Sample Measurements

The same precision loading stage as for the test described in section 2.1 was used for compression testing here. The sample is mounted by a cyanoacrylate adhesive to the compression anvil. A Lithium Niobate sample was used as the counterface and adhered with cyanoacrylate to the opposite compression anvil. The initial position of the compression test is when the sample and the counterface are brought into incipient contact with one another, as observed by the digital microscope mounted above the loading stage. Six compression cycles, with prescribed displacements of 100μm to 600μm, with and increment of 100μm, were performed on the sample at a loading rate of 10µm/sec and unloading rate of 1mm/sec. Resistance of the sample before and during the compression test was measured using an electrical circuit described later. Also, CNT array heights, defined by the distance from where the CNT array was attached to the underlying substrate to the free surface, are measured initially and after each loading cycle all across the entire width of the sample surface to obtain statistical significance in the results.

Vertical Sample Measurements

To measure the resistance changes in the vertical sample during compression, polished silica samples were adhered using cyanoacrylate adhesive to the steel compression anvils to create insulated mounting surfaces. The vertical sample was then wax mounted to one silica covered

anvil. Compression tests with prescribed displacement of 100μm to 400μm with an increment of 100μm were performed on the sample, yielding four cycles total. Every compression cycle begins when the other side of the anvil in contact with the sample judging by the digital microscope above the loading stage and ends when the unloading process is finished, during which two sides of the anvil will separate from each other for a distance same as the compression displacement. The loading rate is 10μm/sec and the unloading rate is 1mm/sec. In the entire compression test, resistance of the sample is being measured using the same circuit as for the lateral sample. The CNT array heights, defined by the distance between where CNT was adhered to the silver epoxy films, were also measured initially and after each loading cycle.

4.3 Resistance Measurements Results

Fig 4.4 and Fig 4.5 show the plots of electrical resistance versus time on varying the applied compressive strain for lateral and vertical sample, respectively. The spikes in the data are due to noise, which needs to be addressed for future experiment. Removing the compressive strain from the CNT array results in a partial recovery of its original shape but with height shortening and buckling forming at the free surface. Likewise, the electrical resistance regained partly of its value but lower than the no load value. This indicates that the electrical resistance and compressive strain responses of the CNT array are partially reversible because of the plastic deformation occurred in the array. Pushparaj [2] observed similar trend. For the lateral sample, resistance was measured perpendicular to the tube growing direction. Electrical current can pass

56

through the sample solely due to nanotube-nanotube interactions, but for the vertical sample; electrical current can also transmit through nanotubes themselves [52]. The resistance change after each loading cycle over the initial resistance ratio *delta R/R* versus strain for the lateral sample and vertical samples are plotted in Fig. 4.6. The slope of d*elta R/R* curve represents sensitivity to strain of the sample. With small strain (less than 10%), the two cases both show low sensitivity to strain but do not have much difference. However, with larger strain, the lateral sample shows a significantly larger sensitivity to strain than the vertical sample which can be seen by comparing *delta R/R* slopes of the two, 2.25 for the lateral sample and 0.44 for the vertical sample. This indicates that the lateral measurement configuration is more sensitive to strain parallel to nanotube growing direction than the vertical measurement configuration.

The decrease in resistance for both cases is attributed to the bending of the CNTs, which results in an overlap of the electron states in adjacent CNT walls, leading to an increase in the accessible number of conduction channels [52]. Another possibility is that on compressive loading, the CNTs bend and the array structure becomes denser; eventually more of the CNTs touch each other leading to lower resistance [2].

4.4 Discussion of Resistance Measurements Results

Lateral Sample

Observing from the geometry change before and after compression of the lateral sample (Fig. 4.7), L_o, length in x-direction and *W*, width in z-direction are assumed to be unchanged. The

57

Height in y-direction is the only geometrical variable during compression. The exact conductive patterns between two electrodes are unknown, and maybe in the way the yellow curves show in Fig 4.7. By definition, resistance is the function of resistivity and the sample geometry. Due to the complex structural change in the array during compression, not only the geometry changed, but also resistivity may have changed as well because if assuming resistivity remains constant, the geometry change in the lateral sample will cause resistance change in the opposite way to current results from the equation:

$$R = \rho \frac{L}{A} = \frac{\rho L_o}{H_i W} \qquad (1)$$

where ρ is the resistivity of the sample. Thus, the results must be a combination effect of both resistivity and sample geometry. In order to explore how the two variation parameters affect the resistance change, an 2-D model of the electric field in the CNT array was simulated in Fig. 4.8, where L denotes conductive path from one electrode to the other, which is the longest linear way electrons can go through the array so that geometry effect can be reflected by the resistance change to the largest extent. The conductive path is assumed to remain the same way across the whole width W in z-direction of the sample. L then can be represented by:

$$L = \sqrt{L_o^2 + 4H_i^2} \qquad (2)$$

where, L_o is length in x-direction which is assumed to be unchanged and H_i is the array height

58

after each loading cycle.

Resistivity ρ must be changing corresponding to the applied strain as discussed above but in an unknown way. Assuming ρ is a function of the applied strain as:

$$\rho = a + b\varepsilon + c\varepsilon^2 + d\varepsilon^3 + e\varepsilon^4 + \ldots\ldots\ldots\ldots \quad (3)$$

where a, b, c, etc are constants need to be determined, ε is the applied strain which can be shown as $\varepsilon = \delta/H$, and H are the prescribed compressive displacement and initial array height of each loading cycle respectively. The applied compressive strain to the sample is so small (max 0.21) that higher order terms in equation (3) can be neglected. Equation (3) can be rewritten as:

$$\rho = a + b\varepsilon \quad (4)$$

Plugging equations (4) and (2) in to equation (1), the resistance R can be shown as:

$$R = \frac{(b\varepsilon + a) \cdot \sqrt{L_o^2 + H_i^2}}{W \cdot H_i} \quad (5)$$

where constant a is the initial resistivity and constant b is the resistivity change with respect to strain. By fitting the constructed model with the experiment results, constant a is determined to be 15.6 Ω-mm and b equals to -19.5 Ω-mm. Since a denotes the initial resistivity of the array, it

59

is a unique solution. Constant b can have deviation of 0.2 to still well fit the experimental data. The fitting results captured the experimental data which is shown in Fig 4.9, which justified the proposed model indicating that the resistance change is a combination effect of both resistivity and geometry change of the CNT array.

Vertical Sample

For the vertical sample (Fig. 4.10), the conductive path is theoretically thought to be along the CNTs growing direction (Y-axis) perpendicular to the underlying surface. Areas (X-Z plane) of both top and bottom surfaces of the array are assumed to be unchanged during compression. After compressive loading cycles, the array height (L_i) is the only geometrical variable of the CNTs array. By definition, $R = \rho L_i/A$ [53], where ρ is resistivity of the sample and A is the array surface area (X-Z plane). The electrical resistance versus array height for each loading cycle is plotted in Fig. 4.11, which shows that with decreasing of the array height, electrical resistance decreases correspondingly, but the two are not in a linear relationship which indicates that when strain caused array height shortening reached a certain value, resistivity is changed causing the deviation of the resistance decreasing trend since array surface area A is assumed unchanged. By taking linear regression of the curve composed of the first three data points and the curve composed of the last three data points respectively, slopes, $S= R/L_i= \rho /A$ of the two curves can be obtained. If taking the slope S times the surface area A, which is measured to be 8.4 mm^2, the resistivity of the array can be calculated to be changing from 40.08 Ω-mm to 16.33 Ω-mm, which is due to the array structural disorder and bending of nanotubes during compression,

60

though the exact relationship between which and the resistivity change needs to be further explored. The array height decreasing and the increasing of the resistivity together result in the decreasing of the array electrical resistance.

Applied compressive strain in CNTs growing direction will cause electrical resistance decreases both perpendicular and parallel to the compression direction which may be due to resistivity change of the array. Results of proposed model for the lateral sample case captured experimental data and analysis to the vertical sample resistance change shows geometry change is not the only contributor, which further confirmed the assumption.
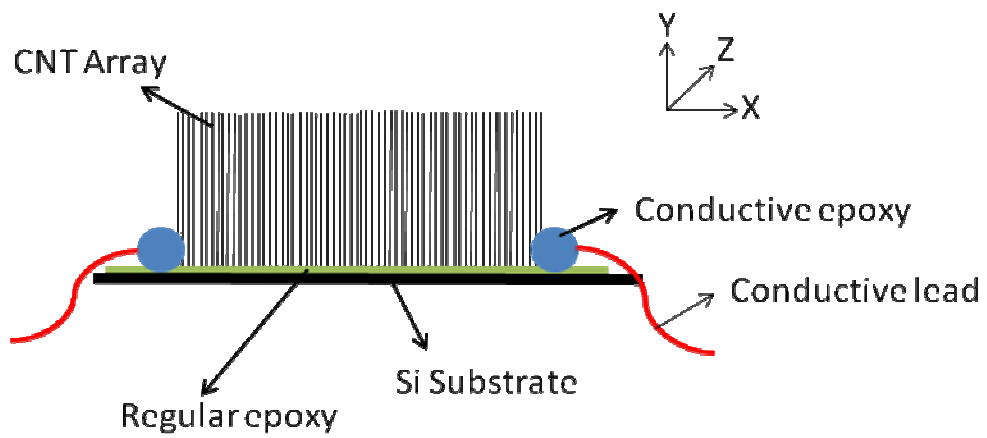
Fig 4.1- Lateral sample side view
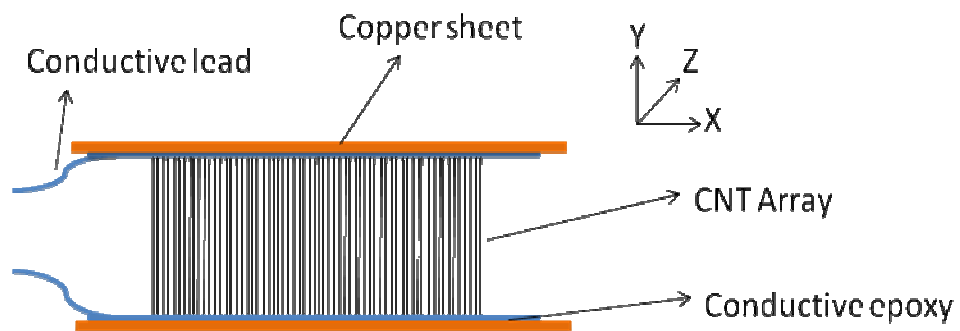
Fig 4.2 - Vertical sample side view
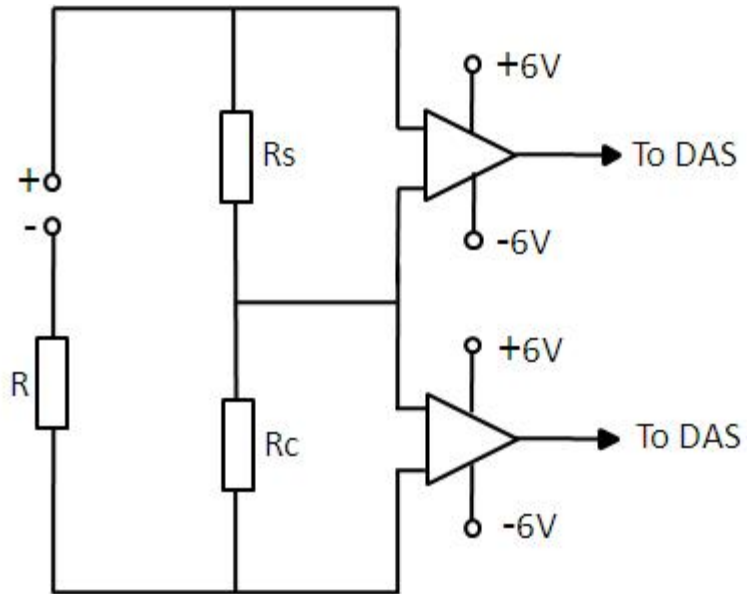
Fig. 4.3 - Diagram of the CNT array dynamic resistance measurement circuit. Voltage signal of the circuit is transmitted to the DAS (Data Acquisition System).
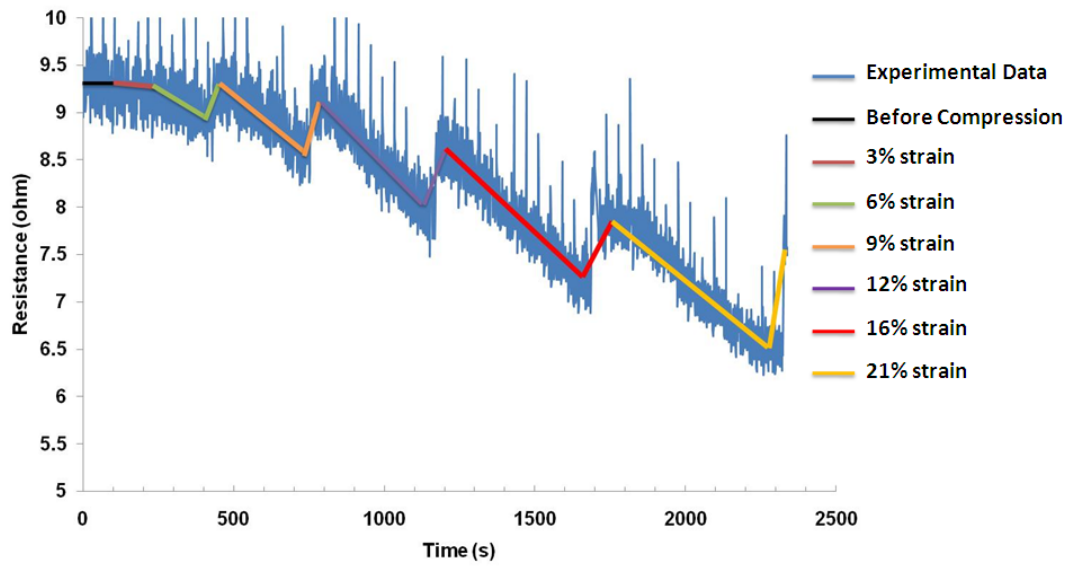
Fig. 4.4 - The plot of electrical resistance vs time on varying the applied compressive strain for the lateral sample
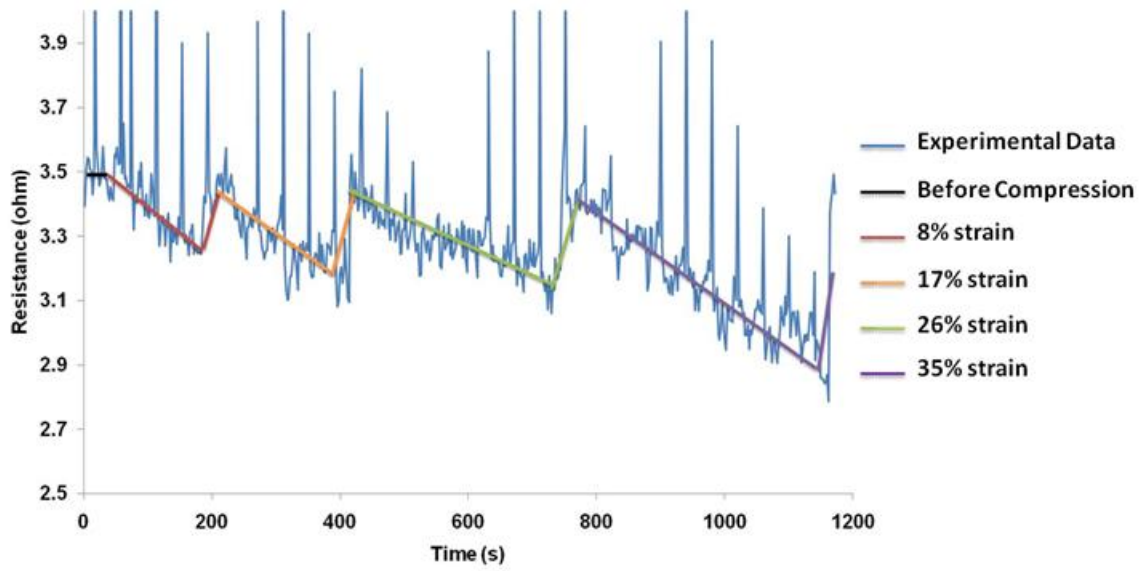
Fig. 4.5 - The plot of electrical resistance vs time on varying the applied compressive strain for the vertical sample.
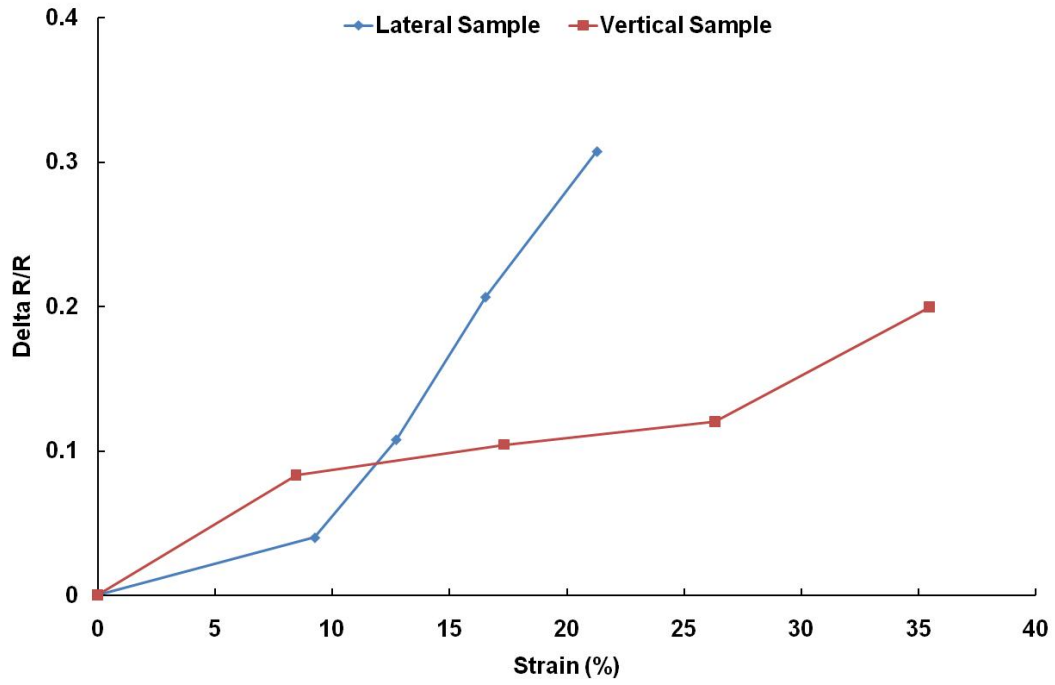
Fig. 4.6 – Resistance change over the initial resistance ratio vs. applied strain for both lateral and vertical sample
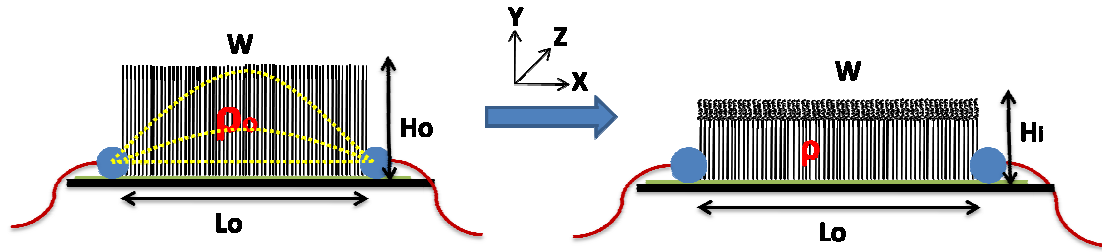
Fig. 4.7 – Lateral sample geometry evolution before and after compression. W is the width in z-direction, ρ_o and ρ represent resistivity before and after compression, L_o is the length in x-direction and H_o/H_i are array heights
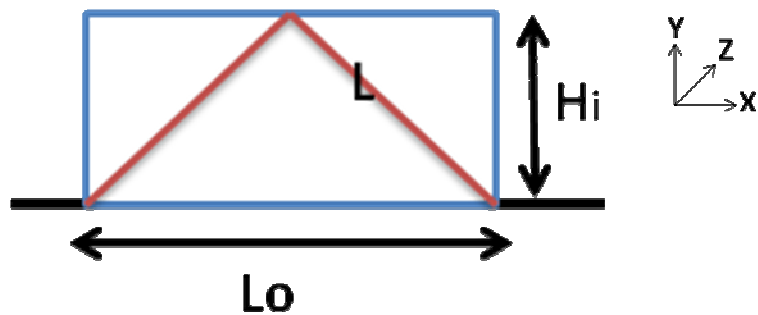
Fig. 4.8 – 2-D Conductive path model of the Lateral sample. L denotes the length of the conductive path, which is from one electrode passing the middle of the array free surface to the other electrode; the blue box represents the CNT array.
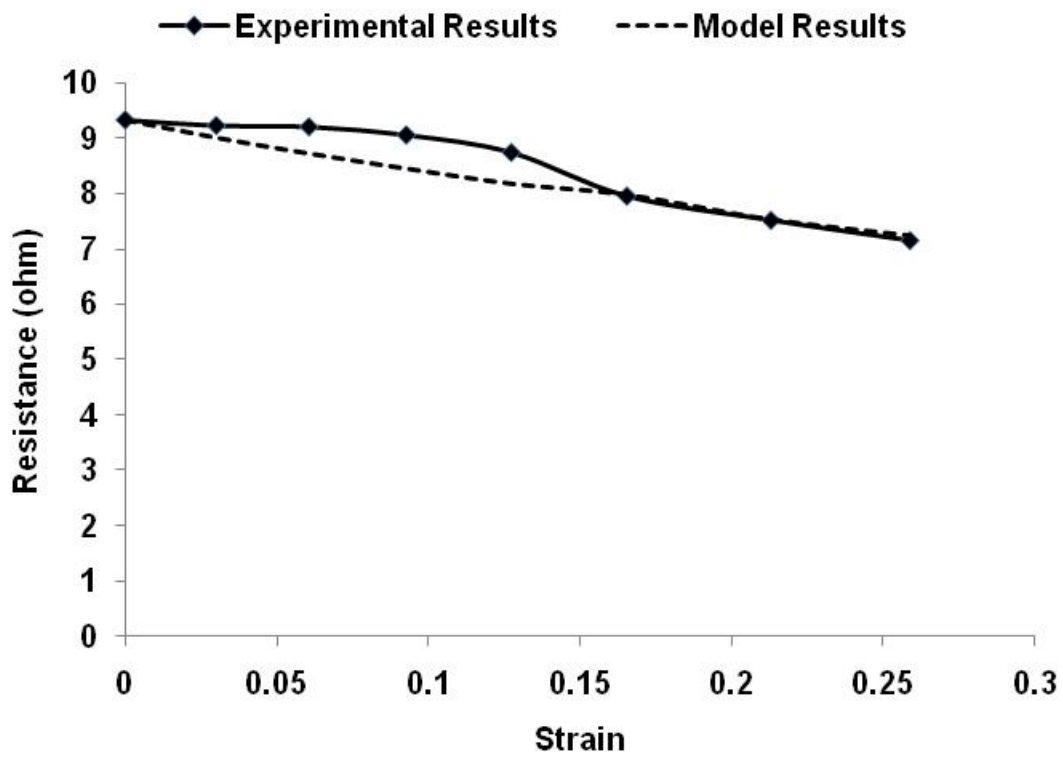
Fig. 4.9 –Comparison of resistances change with applied strain between experimental and model results.
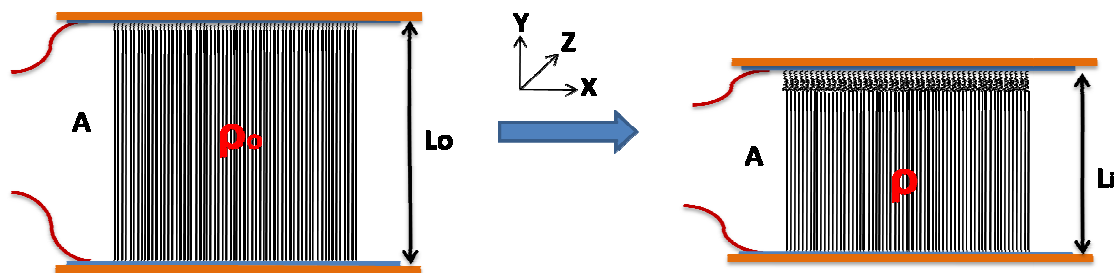
Fig. 4.10. Vertical sample geometry evolution before and after compression. A is the area in z-direction, ρ_o and ρ represent resistivity before and after compression, L_o and L_i are array heights in x-direction
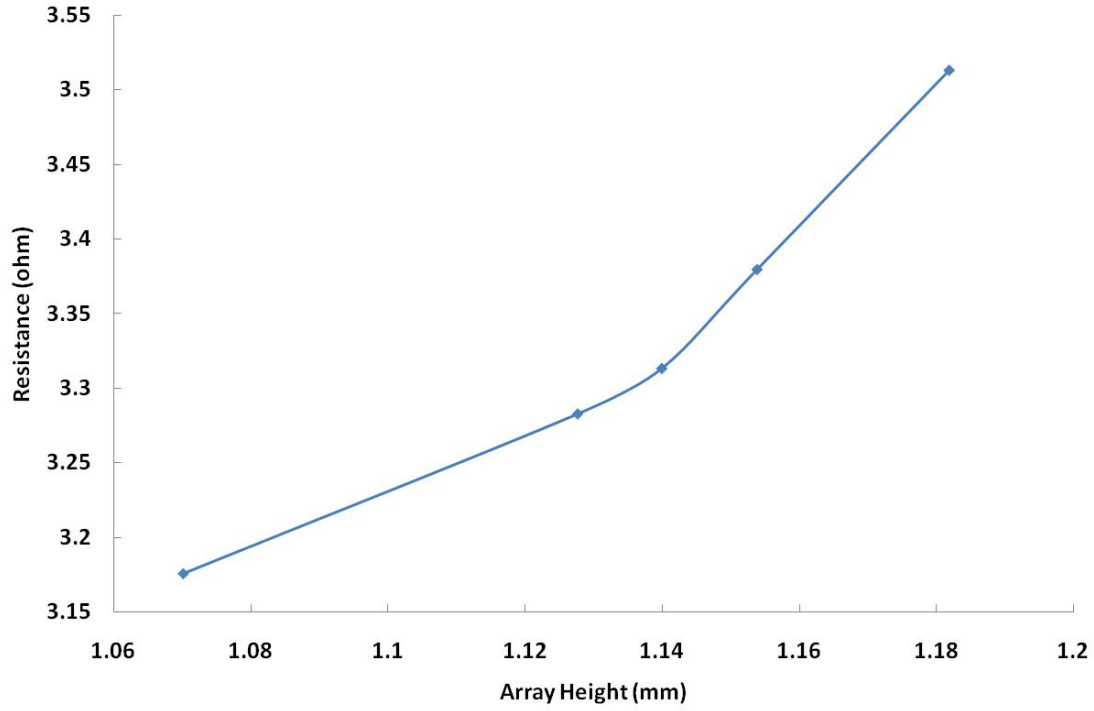
Fig. 4.11 – Electrical resistance vs array height of the vertical sample. The slope of the curve decreases from 4.8Ω–mm to 1.9Ω–mm indicating a resistivity drop

Chapter Five – Conclusions:

Low cycle compression of VACNT array:

- The buckling region growth showed a dependency on the applied displacement indicating a critical value of ~5.5% for compressive strain where buckling remains within a controlled region versus uncontrolled growth. For low displacements, evidence of buckling compaction was observed that was not present in larger applied strains further demonstrating the displacement dependency.

- Counterface material with small elastic modulus will absorb strain energy when using as a compressive counterface, which does not happen for hard materials. ~32% of total array height difference when compressed by counterfaces with different elastic modulus indicating a counterface material dependency of the compressive response of the CNT array.

Characterization of VACNT array by nanindentation:

- The indentation experiments indicate elastic modulus of VACNT array of 12.7 +/- 0.3 MPa for the uncompressed samples and 13.9 +/- 2.4 MPa and 14.8 +/- 1.0 MPa for the compressed samples (δ= 50 and 200 μm, respectively)and also indicate that VACNTs

73

arrays compressed by Gel Polymer for 100μm under the same loading conditions will have surface stiffness of 12.19+/-1.16 MPa and 25.32+/-5.74 MPa for LiNbO$_3$ compressed case.

Characterization of VACNT array by Raman Spectroscopy:

- Raman Spectroscopy in the buckled and unbuckled regions shows that applied compressive strain to the VACNTs arrays will cause more nanotube-nanotube interactions in the buckled region than the unbuckled region, which will result in the abbreviations of C-C bond reflected by the up shift of the G-band peak on the spectra. The sp^2 symmetry of individual nanotubes is not affected much by the applied strain . G-band peak variations also occur within the buckled region which may be due to the difference of deformations along the tube direction or due to variations of the nanotube-naotube interactions within the buckled region.

Electrical Resistance Measurement of VACNTs array under compression:

- With increasing of the applied compressive strain, electrical resistance of the CNT array (both in the vertical or lateral direction) will decrease correspondingly because of sample geometrical change and structural change caused resistivity decrease, ~27% for the lateral sample and 60% for the vertical sample. Also, electrical resistance of the VACNTs array is partially reversible with releasing of the load. Because of the plastic deformation occurred in the array, resistance will not regain to its original value. Multiple loading cycles to the sample results in the overall decreasing of the resistance.

Chapter Six – Future Work:

Future works for experimental improvements or more explorations on VACNT arrays compressive response include:

- *Compression test:* Varying the loading rate, initial array height one parameter a time to see how these changes will affect the buckling length and array height evolution. Instead of using digital microscope to capture images during the test, if SEM can be used to do so, it will largely improve the length measurement accuracy.

- *Raman Spectroscopy:* Raman Spectroscopy on strained MWCNTs array is still a new and challenging topic due to the multi-wall nanotube structure and the complex nanotube interactions. Performing and analyzing Raman scans precisely on different locations within the buckling region, or on samples compressed by different strain, cycles, counterface material, etc will provide more insight info to understand the strain effect to the array form of MWCNTs.

- *Electrical Resistance Measurement of VACNTs array under compression:* Instead of using silver epoxy as the conductive adhesive to attach CNTs array to the electrodes, use a certain adhesive that is stronger and drying faster since arrays are easily fell off from the substrate when silver epoxy is used. Suggestion: mount the CNT array to the loading

instrument vertically instead of laterally to avoid using adhesives to attach the array to

the electrodes, but this needs materials coated on the array surface to bundle the tubes

together, like a graphene sheet. Design a better way of releasing CNTs array from the

grown substrate and attach it to a new substrate because current method needs to be

super careful or the sample will be damaged very easily. Suggestion: mount CNTs array

samples on a precision controlled stage and then bring the sample to a well fixed thin

but strong wire to cut the array from the grown substrate in order to get a flat array

surface without damaging the array structure. Design a test that can explore how

localized strain can affect the resistance change in both vertical and lateral direction of

the sample. Suggestion: instead of compressing the CNT array to a counterface that can

cover the entire sample surface, indenting into the surface with different sizes of the

indenter or indentation depths Better design the circuit so that it can have higher

measurement resolution since the resistance of VACNTs array is usually very small and

even a smaller resistance change even after high applied strain. More precise

measurement circuit will improve the results accuracy. Suggestions: based on the

current circuit design, increasing the gain factor of the amplifier, build noise prevention

system into the circuit and also reprogramming the Data Acquisition System to improve

its resolution. Current method for measuring resistance of the lateral sample has

problems that electrodes need to be attached via conductive adhesive on the side of the

array which may limit the compressive strain. Suggestions: The four-point probe

method which is designed for measuring resistivity of thin layers may help solve this

problem by having electrodes down on the bottom of the array. .

Bibliography:

[1] Cao A, Dickrell PL, Sawyer WG, Ghasemi-Nejhad MN, Ajayan PM.   Super-compressible foamlike carbon nanotube films.   Science 2005;310:1307-1310.

[2] Pushparaj VL, Ci L, Sreekala S, Kumar A, Kesapragada S, Gall D, Nalamasu O, Pulickel AM, Suhr J.   Effects of compressive strains on electrical conductivities of a macroscale carbon nanotube block.   Applied Physics Letters   2007;91:153116-18.

[3] Xu J, Fisher TS. Enhancement of thermal interface materials with carbon nanotube arrays. Intl. J. Heat and Mass Transfer 2006; 49:1658-1666.

[4] Li C, Chou T-W.   A structural mechanics approach for the analysis of carbon nanotubes. Intl. J. Solids Struct.   2003; 40:2487-2499.

[5] Demczyk BG, Wang YM, Cumings J, Hetman M, Han W, Zettl A, Ritchie RO.   Direct mechanical measurement of the tensile strength and elastic modulus of multiwalled carbon nanotubes.   Mater. Sci. Eng. A.   2002; A334:173-178.

[6] Tersoff J, Ruoff RS.   Structural properties of a carbon-nanotube crystal.   Phys. Rev. Lett. 1994; 73:676-679.

[7] Liu YJ, Chen XL.   Evaluations of the effective material properties of carbon nanotube-based composites using nanoscale representative volume element.   Mech. Mater. 2003; 35:69-81.

[8] Goze C, Vaccarini L, Henrard L, Bernier P, Hernandez E, Rubio A.   Elastic and mechanical properties of carbon nanotubes.   Synth. Metals 1999; 103:2500-2501.

[9] Salvetat JP, Bonard JM, Thomson NH, Kulik AJ, Forro L, Benoit W, Zuppiroli L. Mechanical properties of carbon nanotubes.   Appl. Phys. A 1999; 69:255-260.

[10] Dickrell PL, Sinnott SB, Hahn DW, Raravikar NR, Schadler LS, Ajayan PM, Sawyer WG. Frictional anisotropy of oriented carbon nanotube surfaces.   Tribology Letters 2005; 18:59-62.

[11] Waters JF, Reister L, Jouzi M, Guduru PR, Xu JM.   Buckling instabilities in multiwalled carbon nanotubes under uniaxial compression.   Appl. Phys. Lettrs.   2004; 85:1787-1789.

[12] Yap HW, Lakes RS, Carpick RW.   Negative stiffness and enhanced damping of individual multiwalled carbon nanotubes.   Phys. Rev. B (2008); 77:045423-1-7.

[13] Yu MF, Lourie O, Dyer MJ, Moloni K, Kelly TF, Ruoff RS. Strength and breaking mechanism of multiwalled carbon nanotubes under tensile load.   Science 2000; 287:637-640.

[14] Thostenson ET, Chou T-W.   Nanotube buckling in aligned multi-wall carbon nanotube-reinforced composites.   Carbon 2004;42:3015-3018.

[15] Moniruzzaman M, Winey KI.   Polymer nanocomposites containing carbon nanotubes. Macromolecules 2006; 39:5194-5205.

[16] Gibson RF, Ayorinde O, Wen, Y.   Vibrations of carbon nanotubes and their composites: A review.   Comp. Sci. Tech.   2007; 67:1-28.

[17] Ajayan PM, Suhr J, Koratkar N.   Utilizing interfaces in carbon nanotube reinforced polymer composites for structural damping.   J. Mater. Sci.   2006; 41:7824-7829.

[18] Musso S, Giorcelli M, Pavese M, Bianco, S, Rovere M, Tagliaferro A.   Improving macroscopic physical and mechanical properties of thick layers of aligned multiwall carbon nanotubes by annealing treatment.   Diamond and Related Materials 2008; 17:542-547.

[19] Yunus EM, Spearing SM, McBride JW.   Investigation of gold sputter coated vertically aligned multi-walled carbon nanotubes for RF MEMS contact surfaces.   In Microelectromechanical Systems-Materials and Devices II, edited by Spearing SM, Vengallatore S, Sheppard N, Bagdahn J. Matls. Res. Soc. Proc.   2009; 1139:GG05-04.

[20] Johnson RD, Bahr DF, Richards CD, Richards RF, McClain D, Green D, Jiao J. Thermocompression bonding of vertically aligned carbon nanotube turfs to metalized substrates.   Nanotechnology 2009; 20:65703.

[21] Suhr J, Victor P, Ci L, Sreekala S, Zhang X., Nalamasu O, Ajayan PM.   Fatigue resistance of aligned carbon nanotube arrays under cyclic compression.   Nature Nanotechnology 2007; 2:417-421.

[22] Wirth CT, Hofmann S, Robertson J.   Surface properties of vertically aligned carbon nanotube arrays.   Diamond and Related Materials 2008; 17:1518-1524.

[23] Ci L, Suhr J, Pushparaj V, Zhang X, Ajayan PM.   Continuous carbon nanotube reinforced composites.   Nano Letters 2008; 8:2762-2766.

[24] Cao A, Veedu VP, Li X, Yao Z, Ghasemi-Nehjhad MN, Ajayan PM.   Multifunctional brushes made from carbon nanotubes.   Nature Materials 2005; 4:540-545.

[25] Liu Y, Qian W, Zhang Q, Cao A, Li Z, Zhou W, Ma Y, Wei F.   Hierarchical agglomerates of carbon nanotubes as high-pressure cushions.   Nano Letters 2008; 8:1323-1327.

[26] Zbib AA, Mesarovic SD, Lilleodden ET, McClain D, Jiao J, Bahr DF. The coordinated buckling of carbon nanotube turfs under uniform compression.   Nanotechnology 2008; 19:175704.

[27] Tong T, Zhao Y, Delzeit L, Kashani A, Meyyappan M, Majumdar A.   Height independent compressive modulus of vertically aligned carbon nanotube arrays.   Nano Letters 2008; 8:511-515.

[28] Deck CP; Flowers J; McKee GSB; Vecchio K.   Mechanical behavior of ultralong multiwalled carbon nanotube mats.   Appl. Phys. Lettrs.   2007; 101:23512.

[29] McCarter CM, Richards RF, Mesarovic SDj, Richards CD, Bahr DF, McClain D, Jiao J. Mechanical compliance of photolithographically defined vertically aligned carbon nanotube turf.   J Mater. Sci.   2006; 41:7872–7878.

[30] Misra A, Greer JR, Daraio C.   Strain rate effects in the mechanical response of

polymer-anchored carbon nanotube foams.   Adv. Matls.   2009; 21:334-338.

[31] Pathak S, Cambaz ZG, Kalidindi SR, Swadener JG, Gogotsi Y.   Viscoelasticity and high buckling stress of dense carbon nanotube brushes.   Carbon 2009; 47:1969-1976.

[32] Kavan L., Rapta P., Dunsch L., Bronikowski M.J., Willis P., Smalley R.E., J. Phys. Chem. B,105 (2001), 10764.

[33] Alvarez L., Righi A., Guillard T., Rols S., Anglaret E., Laplaze D., Sauvajol J.-L., Chem.Phys. Lett., 316 (2000), 186.

[34] Astakhova T.Yu., Vinogradov G.A., Menon M., Russian Chem. Bull., Int. Ed., 52 (2003), 823.

[35] Dresselhaus M.S., Dresselhaus G., Jorio A., Souza Filho A.G., Pimenta M.A., Saito D.R.,Acc. Chem. Res., 35 (2002), 1070.

[36] Richa Sethi, Andrew R. Barron. Characterization of Single-Walled Carbon Nanotubes by Raman Spectroscopy. , Connexions module: m22925, April, 2009

[37] S. Costa, E. Borowiak-Palen*, M. Kruszyńska, A. Bachmatiuk, R. J. Kaleńczuk Characterization of carbon nanotubes by Raman spectroscopy. Materials Science-Poland, Vol. 26, No. 2, 2008

[38] Mildred S. Dresselhaus, Ado Jorio, Mario Hofmann, Gene Dresselhaus, and Riichiro Saito. Perspectives on Carbon Nanotubes and Graphene Raman Spectroscopy. Nano Letters, 2010, 10,751-758

[39] Sishen Xie, Wenzhi Li, Zhengwei Pan, Baohe Chang, Lianfeng Sun. Carbon Nanotube arrays. Materials Science and Engineering A286 (2000) 11–15

[40] Rajay Kumar and Stephen B. Cronin. Raman scattering of carbon nanotube bundles under axial strain and strain-induced debundling. Physical Review B75, 155421, 2007

[41] Anyuan Cao, Vinod P. Veedu, Xuesong Li, Zhaoling Yao, Mehrdad N. Ghasemi-Nejhad And Pulickel M. Ajayan, Multifunctional brushes made from Carbon nanotubes. nature materials Vol 4,July 2005.

[42] Wu T-C, Chang S-H.   Temperature enhanced growth of ultralong multi-walled carbon nanotube forests.   Current Applied Physics   2009;9:1117-1121.

[43] Simonetta Grilli, Pietro Ferraro, and Paolo De Natale. Surface nanoscale periodic structures in congruent lithium niobate by domain reversal patterning and differential etching. Applied Physics Letter 87, 233106; 2005

[44] Properties of Lithium Niobate, EMIS Data Reviews Series No. 5 (INSPEC, London 1989).

[45] NT-MDT Co.   Gel properties technical data sheet TD026B

[46] Keyence VHX-500 Manual

[47] Doener MF, Nix WD.   A method for interpreting the data from depth-sensing indentation instruments.   J. Matls. Res.   1986;1:601-616.

[48] Johnson KL.   Contact Mechanics.   Cambridge; 1987.

[49] A Jorio, M A Pimenta, A G Souza Filho, R Saito, G Dresselhaus and M S Dresselhaus. Characterizing carbon nanotube samples with resonance Raman scattering. New Journal of Physics 5 (2003) 139.1–139.17.

[50] Xinluo Zhao and Yoshinori Ando, Lu-Chang Qin, Hiromichi Kataura and Yutaka Maniwa, Riichiro Saito. Multiple splitting of G-band modes from individual multiwalled carbon nanotubes. Appl. Phys. Lett., Vol. 81, No. 14, 30 Sep,2002.

[51] S. M. Bachilo, M. S. Strano, C. Kittrell, R. H. Hauge, R. E.Smalley, and R. B. Weisman. Science 298, 2361 _2002_

[52]. V. Semet, V. T. Binh, D. Guillot, K. B. K. Teo, M. Chhowalla, G. A. J.Amartunga, W. I. Milne, P. Leganeux, and D. Pribat, Appl. Phys. Lett. 87, 223103 _2005_.

[53]. Ward, MR, Electrical Engineering Science, McGraw-Hill, 1971